



Bubble eruptions in a multilayer Hele-Shaw flowAhmed Al Brahim ^{1,2} and Sigurdur T. Thoroddsen ^{1,*}¹*Mechanical Engineering, Division of Physical Science and Engineering, King Abdullah University of Science and Technology (KAUST), Thuwal 23955-6900, Saudi Arabia*²*Oil and Gas Networking Integrity Division, Research and Development Center, Saudi Aramco, Thuwal 23955-6900, Saudi Arabia*

(Received 27 August 2021; accepted 24 February 2022; published 4 April 2022)

We study the dynamical rearrangement of gravitationally unstable multilayer fluid inside the narrow vertical gap of a Hele-Shaw cell. Four layers of immiscible fluids are superposed inside the cell, which is subsequently turned over. We vary the fluid properties and the relative thicknesses of the layers. One of the layers is air, the others are immiscible liquids: olive oil, water-glycerin mixture, and perfluorohexane. The concentration of the glycerin-water mixture is used to vary its viscosity. We classify various different dynamics of stirring and breakthrough of adjacent layers. We note a prominent phenomenon, where an air finger breaks through the high-viscosity layer to erupt as a hemisphere into the lower-viscosity perfluorohexane layer above it. These eruptions have a periodic neck pinch-off accompanied with high-speed airflow which breaks up some of the low-viscosity liquid to eject a spray of fine droplets. We use high-speed video to characterize the details of the eruptions and how wetting, contact lines and three-dimensionalities play a key role. We also investigate the center-of-mass trajectories for each layer and notice counterflows, where the center of some layers can temporarily move against buoyancy. The top and bottom layers can interchange by channeling through the intermediate layers, which subsequently overturn on longer timescales. We also point out some unexpected dynamics occurring in the triple- and four-phase interactions. Specifically, droplet motions are as much affected by local viscosity as by the density gradients.

DOI: [10.1103/PhysRevE.105.045101](https://doi.org/10.1103/PhysRevE.105.045101)**I. INTRODUCTION**

In many natural phenomena and industrial applications multiphase flow is confined to move through narrow vertical channels. During these confined flows in narrow ducts immiscible liquid layers can overturn to produce inverted density profiles, where heavy fluid resides above a lighter one, thereby forming configurations susceptible to gravity-driven Rayleigh-Taylor instability. In geophysical flows these configurations are relevant for multiphase flow of gas and molten lava in volcanic dykes. This emerges when gas escapes under reduced hydrostatic pressure, subsequently manifest by eruptions of lava fountains [1]. On a much larger geological length-scales, from the motions derived from continental drift, the subduction of oceanic plates under the continental plate entraps water-rich crust into the mantle, which subsequently heats up and expands, rising through planar vertical fractures in the crust, to form a range of volcanoes, e.g., along the *ring-of-fire*.

Multiphase flow in narrow channels also occurs in many chemical engineering processes, such as distillation. Enhanced oil recovery often uses fracking and reservoir flooding with water, giving a plethora of possibilities for the emergence of unstable multiphase flows in narrow fractures.

Instabilities can also occur in horizontal flows, or immiscible flow without a density difference. These arise for example from changes in the viscosity of pressure-driven flows, i.e., the Saffman-Taylor instability, when a lower-viscosity fluid pushes on a more viscous layer. Saffman and Taylor [2] studied the properties of this instability that now bears their name. They were able to develop analytical solutions for the shape and stability of the most dominant finger, forming at the interface, but under certain assumptions. Their work has been followed by several others to incorporate factors neglected in their solutions such as the surface tension, surfactants, surface wetting, as well as tackling values outside their parameters limits [3–8]. The basic Hele-Shaw theory is based on a single-phase model of an irrotational 2D flow field [9]. However, multiphase experimental flows in this configuration unavoidably introduce three-dimensionality via interface curvatures, thin wetting films on the glass, or the presence of contact lines. The thickness-profiles of these films have been studied theoretically and experimentally [10,11], as recently reviewed by Shukla *et al.* [12]. Furthermore, flow along curved interfaces can introduce vorticity, which shapes the interface [13,14].

Three-dimensionalities are even more significant herein as the spacing of the glass plates, in our Hele-Shaw device, is rather large. Despite the misnomer, Hele-Shaw devices have

*sigurdur.thoroddsen@kaust.edu.sa

Published by the American Physical Society under the terms of the [Creative Commons Attribution 4.0 International](https://creativecommons.org/licenses/by/4.0/) license. Further distribution of this work must maintain attribution to the author(s) and the published article's title, journal citation, and DOI. Open access publication funded by King Abdullah University of Science and Technology.

been widely used to study fingering and other multiphase phenomena in confined flows. Homsy [15] gives a comprehensive review of these dynamics. The above instabilities are the cause for mediocre oil recovery of the secondary and tertiary oil reservoir flooding processes, where water is injected to displace the viscous oil. To improve this recovery, a thin layer of polymer can be injected before the water with an intermediate viscosity between it and the oil. This layer serves to reduce the jump in the viscosity between the water and oil and can in turn limit instability growth [16].

Tryggvason and Aref [17] studied the true Hele-Shaw flow with numerical simulations using a vortex-in-cell formulation, with the vorticity confined to the interface. Their results are presented for a range of viscosity ratios and effective Bond numbers. They observe a dominant finger like in the Saffman-Taylor experiment, but they also identify regimes with bubbles forming at the tip of the fingers and the appearance of top and bottom asymmetry of the interface structure.

Maxworthy [18] performed seminal experiments with two immiscible fluids in a Hele-Shaw cell oriented at various angles to the vertical, to characterize the nonlinear evolution of the fingers. His device is of similar overall dimensions as ours, but with a much narrower gap δ of 2.1 mm. He observed the growth of a large dominant finger which overtakes other nearby ones. He statistically characterized the spacing, splitting, and numerous other properties of their evolution.

Maher [19] has similarly investigated the viscous fingering patterns between two immiscible liquids in an overturned Hele-Shaw cell. He focused on the viscosity contrast between the liquids which he was able to control by changing the temperature. He determined that at a low viscosity contrast, the adjacent viscous fingers have very limited interaction and continue to grow with time. As the viscosity contrast increases, more fingers coalesce. Finally, he established a power-law relationship between the length of the longest finger with time for different viscosity contrasts.

While the flow within a Hele-Shaw cell is typically analyzed in two dimensions, it is still impacted by three dimensional factors across the cell gap. Park and Homsy [4] have established that as one fluid penetrates into the other, thin films of the penetrated liquid will remain that wet the cell walls. They determined that at a low capillary number Ca the thin film will cause a pressure drop across the leading interface. Helpert and Gaver [20] have studied this thin film over a wide Ca range. They observed that the pressure drop will increase with Ca for Ca values less than twenty. Beyond this range the pressure drop is not effected by the increase of Ca . They have also established that the shape of the finger across the cell gap stabilizes for $Ca \simeq 20$.

Ledesma-Aguilar *et al.* [21] have shown that, at very low Ca , the depth of the penetrating finger, across the cell gap, will decrease if the aspect ratio between the cell gap and width increases. They have also determined that, at a low Ca and a small aspect ratio, the thin-film thickness will increase with the increase in the viscosity contrast between the fluids.

The stability of multilayer systems has been less studied, besides the continuing work of Daripa and coworkers [22–29] who have performed a series of theoretical studies of the linear stability of multilayer pressure-driven linear and radial Hele-Shaw systems. This formulation is of relevance to enhanced



FIG. 1. Photograph of the Hele-Shaw device, filled with three liquid layers and air on top, before the overturn. The cell can be rotated about the pivot points at the center of the sides. The video camera is prefocused and mounted on a sturdy tripod.

oil recovery by water injection into reservoirs, with the aim of minimizing or suppressing the Taylor-Saffman instability. This is done by optimizing the arrangement of intermediate-viscosity layers between the primary phases. This includes spatially varying viscosity of various functional forms. The sophisticated formulation is purely two-dimensional and limited to small-amplitude disturbances.

In this research, we have utilized a large Hele-Shaw cell filled with multiple layers of immiscible fluids to investigate their dynamical rearrangement after the cell is rotated upside down around its horizontal pivot. The fluids that we have filled the cell with are air and three immiscible liquids: olive oil, a water-glycerin mixture and the densest phase of perfluorohexane (PP1). We have varied the relative thicknesses of these layers as well as the concentration of the water-glycerin mixture to obtain a wide range of different viscosities. In our arrangement, the middle layers are the most viscous, with the formation of air fingers penetrating the higher-viscosity middle layers and erupting into the low-viscosity top PP1 layer. The dynamics of these eruptions is the focus of this work.

The paper is organized as follows: In Sec. II we describe the experimental setup, the fluid properties, the Hele-Shaw device and the video-imaging used. Section III introduces the governing parameters and Sec. IV the basic instabilities of the fluid motions induced by the cell rotation. It also describes our eruption model. Section V shows the overall results of the experiments for numerous configurations, while focusing on the eruptions of the air pockets through the viscous layer. Finally, Sec. VI discusses and summarizes the main findings.

II. EXPERIMENTAL SETUP

A. Hele-Shaw device

Figure 1 shows a photograph of the experimental setup, which consists of a large Hele-Shaw device, with a horizontal

TABLE I. Physical properties of the liquids in experiments.

	ρ (kg/m ³)	σ (mN/m)	μ (mPa s)
Perfluorohexane (PP1)	1710	11.9	0.81
Olive oil	919	32.0	118
Water	998	72.9	0.977
Glycerine 65%	1181	66.6	62
Glycerine 75%	1205	65.8	80.5
Glycerine 80%	1217	65.4	128
Glycerine 95%	1251	64.3	596
Glycerine 96.7%	1254	64.1	756
Glycerine	1260	63.9	1296
air	1.2	—	0.018

pivot, which allows it to be flipped over vertically. The inside dimensions of the cell are: width $W = 950$ mm, height $H = 550$ mm, and the gap width is estimated to be $\delta = 3.95$ mm. The glass plates are 18.8 mm thick and are held in place inside a stainless steel frame, with a stiff silicon rubber spacer to keep the spacing uniform and to prevent the cell from leaking. The thick glass plates minimize enlargement in the gap between the plates from changes in the hydrostatic pressure.

The initial air eruptions tend to occur near the center-line of the cell, which commonly occurs in narrower cells, owing to the boundary effects. Here the cell is quite wide and another possibility might be a variable gap thickness. It is therefore of interest to estimate how much the glass plates bend by hydrostatic pressure, which will slightly increase the spacing of the plates at the center of the cell. Considering linear elasticity, these deformations can be estimated from classic plate theory. Using the average hydrostatic pressure p_{ave} immediately following the overturn the deformation perpendicular to the glass at the center of the cell, follows the formulation of Imrak and Gerdemeli [30]: $\Delta z = 3\pi WH^3(1 - \nu) p_{ave} / (8ET^3)$, where E is the Young modulus for the glass, T the thickness of the glass plates and ν is its Poisson ratio. This gives a maximum plate displacement Δz of only $300 \mu\text{m}$, which will not significantly affect the dynamics.

In the current experiments we use an air layer and three separate immiscible liquid layers, where the heaviest is perfluorohexane (PP1), the second layer is more viscous, consisting of water-glycerin (colored blue), where we have varied the viscosity between experiments by changing the glycerin concentration. The third liquid layer is olive oil, which is colored red. This oil was selected as it is much easier to clean than for example silicone oil. Perfluorohexane is an inert liquid which is not easily colored and therefore remains opaque. It can however be distinguished from the air in the video files, by its motion and the dark interface between them. Figure 2(a) shows a photograph of these layers after they have been filled into the cell, before the turn-over.

Table I lists the liquid properties of the different fluid layers. The unstable density profile following the overturn is plotted in Fig. 3(a). The largest jump in density is between the gas and the liquid (olive oil) above the air layer, which drives the fastest initial motions. Indeed, the Rayleigh-Taylor instability of this layer already starts during the

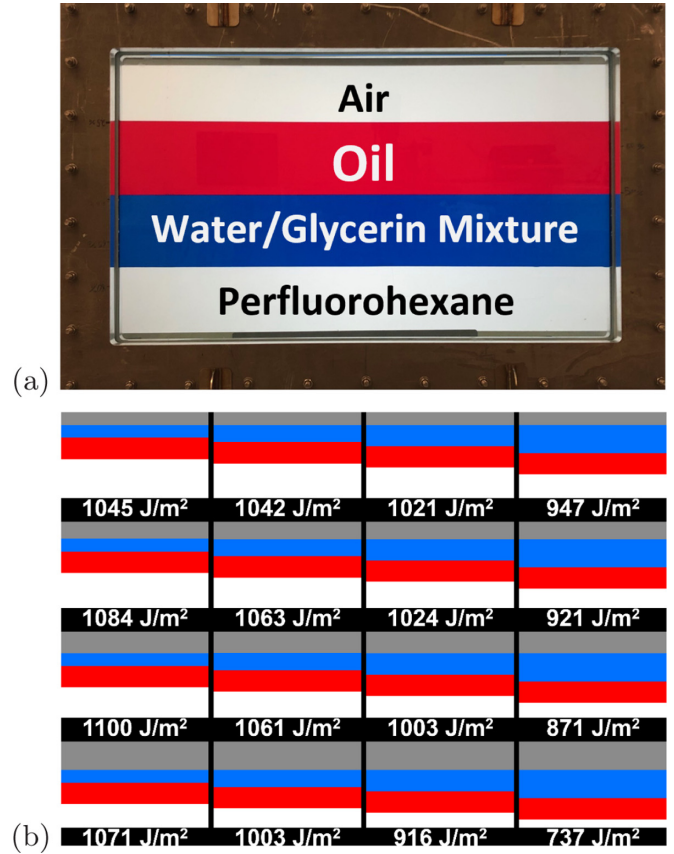


FIG. 2. (a) Photograph of the four hydrostatically stable immiscible fluid layers inside the Hele-Shaw device, following its filling, but before the device is rotated up-side-down around the horizontal pivot. (b) The matrix of 16 different layer thicknesses used in the experiments. The unstable vertical arrangement shows the fluid layers immediately following the overturning of the Hele-Shaw cell. The white region indicates the air layer, red the olive oil layer, blue the glycerin-water mixture, and on top the heaviest gray layer, which is the perfluorohexane (Flutech PP1). Each row shows a particular thickness of the PP1 (gray) layer (15, 20, 25, and 33%), while the different columns show an increasing thickness of the blue glycerin-water layer by the same percentages of 15, 20, 25, and 33%. The air layer becomes thinner to compensate for the increased combined thickness of the glycerin-water and PP1 layers, while the red olive oil layer is the same thickness throughout all experiments, at 25% of the total height. The total input potential energy per unit width and depth, available to drive the motions following the overturn [Eq. (2)], is stated beneath each configuration, where we use the density of pure glycerine for the blue layer.

turn-over of the cell, which takes about 1.5 s. The density jump between the three liquids changes slightly with the glycerin concentration, while the changes in viscosity are more significant to the overall motions. Note that the viscosity-axis in Fig. 3(b) is on a log-scale. The different blue hues in the figure show the range of different values of ρ and μ for the water-glycerin layer.

During the motions all the different immiscible fluids come in contact with each other and their interfacial tension is listed in Table II, taken from the literature or measured using the hanging-drop method. Keep in mind that no surfactants are

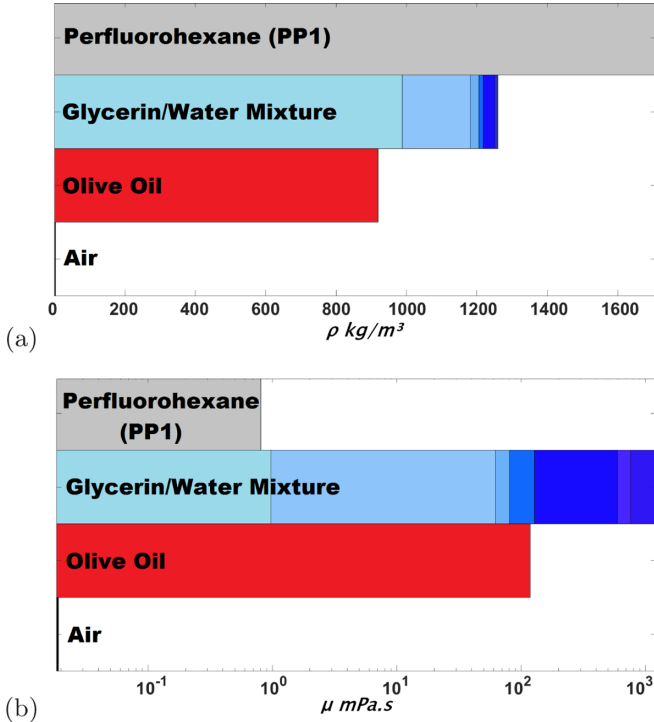


FIG. 3. Schematics showing the vertical distribution of densities and dynamic viscosities of the experimental fluid layers, in the unstable arrangement immediately following the overturning of the cell. (a) Density profile and (b) viscosity profile. The different hues of blue indicate the variability for different mass fraction of the glycerin in the glycerin-water mixtures. The viscosity changes strongly with glycerin content, from 1 to 1296 cP. Note that the pure glycerin viscosity is highly influenced by the temperature. The experiments were conducted in an air conditioned laboratory where only slight temperature variation is to be expected. This also changes, to a lesser degree, the density of the mixture, from 1000 to 1260 kg/m³. The fluid properties of the other layers remain constant, as listed in Table I.

added to stabilize the drops and bubbles generated by the dynamics.

B. The video imaging

To view the flow evolution in the entire cell, we use a *Red Cinema Epic-M Dragon 6k* color video-camera with 6144 × 3072 pixels, using a frame-rate of 82.8 fps. We use a Nikon 55 mm lens, which gives a pixel resolution of about 158 μm/px. Figure 4 shows a typical video frame from this camera. It includes an air-eruption through the glycerin-water

TABLE II. Surface tension between liquid layers in mN/m.

	Olive oil	Water	Glycerine	PP1
Air	32.0	72.9	63.9	11.9
Olive oil	—	23.6	17.2	11
Water	23.6	—	—	55.8
Glycerine	17.2	—	—	42
PP1	11	55.8	42	—

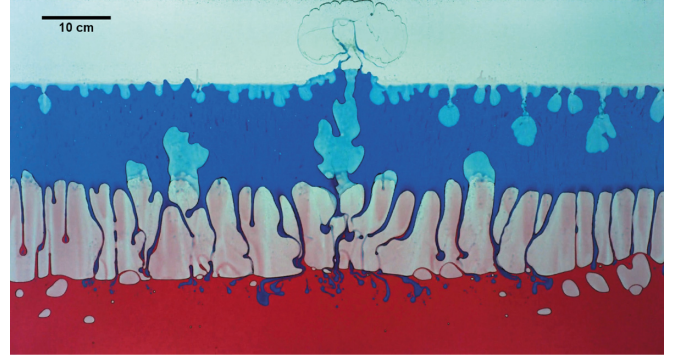


FIG. 4. Multilayer flow-field, with a prominent first eruption, along the centerline, of an air finger into the heavy PP1 top layer. At this stage the red oil layer has fully overturned, replacing the air at the bottom of the cell. Thin streaks of the blue viscous layer have reached through the air layer to the top of the red oil, partitioning the air. Layer thicknesses here are $\Delta H_i = [0.25_a, 0.25_o, 0.25_{97\%g}, 0.25_p]$

layer near the cell centerline—the phenomenon on which this study is focused. These bubble eruptions occur rapidly and required higher frame-rate imaging, which were obtained with a Photron SA-3 color high-speed video camera, at frame-rates between 2000 and 4000 fps, but with a much smaller corresponding pixel areas, ranging from 1000 × 1000 px down to 250 × 250 px at the higher frame-rate. Using the 55 mm lens this gave an image resolution around 200 μm/px.

Limited imaging was done at even higher frame-rates of 12 kfps, using a Photron SA-5 video camera.

III. GOVERNING PARAMETERS

The overall motions are driven by gravity and one way to quantify the strength of the driving force is the potential energy ΔE_p imparted by the rotation of the cell,

$$\Delta E_p = E_{p2} - E_{p1}, \quad (1)$$

where E_{p1} and E_{p2} denote the potential energy, before and after the overturn, each calculated by

$$E_p = \int_0^H \rho(z) g z dz = \frac{g}{2} \sum_{i=1}^4 \rho_i [H_{it}^2 - H_{ib}^2]. \quad (2)$$

The subscripts “it” and “ib” denote the top and bottom heights of layer i , measured from the bottom of the cell. The potential energy of the air layer is insignificant and could be ignored, but plays the key role of displacing the other layers. Figure 2(b) shows a matrix of the different layer thicknesses used in the experiments. The corresponding input driving energies ΔE_p , are written under each configuration. The values are in terms of unit depth and unit horizontal width. The largest change in density occurs when the air replaces one of the liquids. However, note that the largest energy input does not occur for the tallest air layer, but for one of an intermediate height. For example, for a simpler case of only two layers, the maximum increase in ΔE_p would occur for a half-filled cell.

Figure 2(b) shows schematically the relative layer stacking and thicknesses tested. We have systematically varied the thicknesses of the blue glycerin-water layer and the heaviest

gray PP1 layer, with the oil layer kept at constant thickness (25 % of the total height), while reducing the vertical depth of the air layer correspondingly. The layer thicknesses of PP1 and the glycerin-water layers are varied between 15, 20, 25, and 33 % of the total height, as is illustrated in Fig. 2(b). The corresponding extremes in the thickness of the air layer become 9 and 45 %. The relative thicknesses, started from the bottom, are indicated in the text by a bracket notation, e.g., for the top-right case in Fig. 2(b) $\Delta H_i = [0.27_a, 0.25_o, 0.33_g, 0.15_p]$.

In a limited set of experiments we used only three layers, leaving out the olive oil layer, as discussed in Sec. V E.

While the main driving force of the motions is the buoyancy owing to the inverted density profile in the vertical direction, we also see the emergence of pressure-driven flow, which arises from the compression of the air layer by the overlying liquid layers which are slowly pulled down to slightly compress the air. Once the air finger breaks through the glycerin layer, this over-pressure drives rapid airflow through them.

Not only is the density difference between the initially adjacent fluids important, but other pairs of fluids can also come into contact during the motions, following the overturning. In other words, the air layer is initially under the oil layer, but the air bubbles will also pass through the water-glycerin and the perfluorohexane layers, during their rise from the bottom up to the top of the cell. We therefore denote the density and viscosity difference between the adjacent layers as $\Delta\rho_{ij}$ and $\Delta\mu_{ij}$, where i and j indicate the different layers, marked by p (perfluorohexane), g (glycerin-water), o (oil), and a (air).

What forces resist the motions? Inertia and viscous stress and to a lesser extent the surface tension, which are matched to the driving force to obtain the following nondimensional parameters. The Bond number compares the buoyancy and surface tension between layers i and j ,

$$\text{Bo}_{ij} = \frac{\Delta\rho_{ij} g L^2}{\sigma_{ij}}, \quad (3)$$

where σ_{ij} is the surface tension, g is gravity, and L is a characteristic length, e.g., a particular layer height. Based on the typical thicknesses of the heavier layer, i.e., $L = 0.25H$, these Bond numbers are always larger than 600, showing that surface tension does not directly control the overall motions. However, the surface curvature is more dependent on the spacing of the glass plates δ , which suggests a modified definition using two length scales, $\text{Bo}_{ij}^* = \Delta\rho_{ij} g L \delta / \sigma_{ij}$, which reduces the value to $\text{Bo}_{ow}^* = 18$, still limiting the role of the surface tension to shaping the smallest features of the flow, like drops, bubbles, or the tips of extended fingers.

The viscous effects against the inertia forms the Reynolds number, using the narrow width of the channel δ ,

$$\text{Re}_i = \frac{\rho_i \delta U}{\mu_i}. \quad (4)$$

Taking the velocity of the prominent air fingers (later Fig. 9) and the viscosity of the surrounding medium, the large range of glycerin-water concentrations, gives a range of the $\text{Re}_{g/w} = 0.14 \rightarrow 2400$, covering the full range of viscous to inertia dominated motions, as shown in Sec. V B. Keep in mind that

other forces may not be affected by the spacing δ , but by the in-plane extent of the bubble D , such as the buoyancy force.

Following Homsy [15] the modified Darcy-Rayleigh number, compares the relative importance of buoyancy and viscous forces:

$$G = \frac{(\rho_i - \rho_j) g \delta^2}{12(\mu_i + \mu_j) U}. \quad (5)$$

Here we will see a limited range of values $G \sim 0.3$ over a range of viscosities of the glycerin-water layer as we will find $U \sim \mu_g^{-1}$. Only the lowest glycerin concentrations show different behavior.

The difference in viscosity of adjacent layers is also of importance, especially with respect to Taylor-Saffman instability discussed below. Following Tryggvason and Aref [17], we define a viscous Atwood ratio

$$A = \frac{\mu_i - \mu_j}{\mu_i + \mu_j}. \quad (6)$$

For the PP1 versus glycerin-water interface the value of A spans from 0.1 to 1, with increasing glycerin concentration.

The relative strength of surface tension versus viscous stress is characterized by the capillary number,

$$\text{Ca}_i = \frac{\mu_i U}{\sigma}, \quad (7)$$

where μ_i is the dynamic viscosity of layer i . This form of the capillary number contains no length-scale, which assumes that the two forces are subject to the same characteristic length. In our configuration the strength of the viscous stress is primarily caused by the spacing of the glass plates δ , owing to the no-slip boundary condition, when the liquid is in contact with the solid. This spacing will also control the relevant curvature, of the edge of a bubble or immiscible liquid-liquid interface, producing the jump in capillary pressure. However, keep in mind that the glass plates may not be wet with the same liquid which is moving along the center of the channel, as will become evident from the imaging, by dewetting and moving contact lines. These thin films can alter the effective boundary conditions. Such effects have for example been dramatically demonstrated during impacts of high-viscosity drops on lower-viscosity films [31].

Having four different fluids, with their own properties and many possible combinations across these immiscible fluid interfaces, this leads for example to $(n - 1)! = 6$ surface tensions, identified by σ_{ij} , which are listed in Table II. However, many of the underlying physical properties are difficult to vary, such as the densities of the different layers. As explained above, we have herein focused on changing two features: First the relative thickness of the perfluorohexane and water-glycerin layers versus the air layer, while the thickness of the olive oil layer is kept constant at 25 % of the full height. The range of layer thicknesses tested are shown schematically in Fig. 2(b), along with the initial input potential energy. Secondly, we have varied the viscosity of the glycerin-water mixture, by changing the concentration. Herein we investigate how changing these factors affects the observed phenomena.

IV. INTERFACE INSTABILITIES

Following the overturning of the Hele-Shaw cell, we have produced three density interfaces that are unstable to Rayleigh-Taylor instability [32,33]. For the 2D case, all disturbance wavelengths λ are unstable to the inviscid inertial instability, while surface tension stabilizes waves with wave numbers $k = 2\pi/\lambda$ greater than a critical value: $k_c = \sqrt{g(\rho_t - \rho_b)/\sigma_{tb}}$. The exponential growth-rate, as function of k , is given by

$$\alpha = \sqrt{\frac{gk(\rho_t - \rho_b)}{\rho_t + \rho_b} - \frac{k^3 \sigma_{tb}}{\rho_t + \rho_b}}. \quad (8)$$

The fastest growth-rate occurs for wave number $k^* = k_c/\sqrt{3}$, with the corresponding exponentially growing amplitude $A \sim \exp(\alpha^*t)$, with time t , where

$$\alpha^* = \sqrt{\frac{2}{3^{3/2}} \frac{(\rho_t - \rho_b)^{3/2} g^{3/2}}{(\rho_t + \rho_b) \sigma_{12}^{1/2}}}. \quad (9)$$

Here the subscripts t and b refer to the top and bottom layers.

Based on this theory, which ignores viscosity, the bottom air-olive oil interface is the most unstable, followed by the glycerin-water-PP1 interface, while the oil-glycerin-water is the least unstable. The growth rates of these three layers are, respectively: $\alpha_{ao}^* = 45$, $\alpha_{gp}^* = 19$, and $\alpha_{og}^* = 14 \text{ s}^{-1}$. This is indeed what is observed in the experiments where the overturning of the air-oil layer occurs much faster than the other two interfaces. The corresponding fastest growing wavelengths, $\lambda^* = 2\pi/k^*$, are $\lambda_{ao}^* = 20$, $\lambda_{gp}^* = 31$ and $\lambda_{og}^* = 34 \text{ mm}$. Keep in mind that the gap between the glass plates, $\delta = 3.95 \text{ mm}$, is small enough for surface tension to stabilize all wave numbers along the interface in the direction perpendicular to the glass, i.e., $\delta < \lambda^*/\sqrt{3}$.

The above analysis ignores viscosity, which will clearly slows down the motions of the water-glycerol layer, as becomes clear in the overall dynamics below. Including viscosity brings us to the seminal work of Saffman and Taylor [2] and the well-known viscous fingering when lower viscosity fluid is pushed into higher viscosity one, with the associated problems in enhanced oil recovery by water injection into reservoirs. Homsy [15] attributes the explanation of the mechanism to Hill [34] and the solution of the linear stability to Chouke *et al.* [35]. The basic underlying mechanism of the viscous-finger instability is the same for flow in porous media and the Hele-Shaw cell. If one considers a flat interface translating at velocity V owing to pressure gradient under gravity, by Darcy's law the streamwise pressure gradient is $dp/dz = -\mu V/K + \rho g$, where K is the permeability. For the Hele-Shaw with Poiseuille profile this becomes $dp/dz = -12\mu V/\delta^2 + \rho g$. Now we consider a local displacement δz and check whether the net change in the pressure, i.e. $\delta p = (p_2 - p_1) = [12(\mu_1 - \mu_2)V/\delta^2 + (\rho_2 - \rho_1)]\delta z$, is positive. If so the displacement will amplify and cause instability. In purely heuristic terms, if a tongue of low-viscosity liquid penetrates into a higher-viscosity one, the lower pressure drop through this low-viscosity channel makes it energetically beneficial for the subsequent liquid to follow in its path. The second term shows that an opposing density gradient across the interface can overpower this tendency.

The modified rate of growth of disturbances on an interface, with gravity and an imposed pressure gradient which drives a uniform interfacial normal velocity of V becomes [17,18]

$$\frac{12\alpha}{\delta^2}(\mu_i + \mu_j) = \frac{2\pi}{\lambda} \left[\frac{12V}{\delta^2}(\mu_i - \mu_j) + g \Delta\rho_{ij} \sin\theta \right] - \frac{8\pi^3 \sigma}{\lambda^3},$$

where λ is the disturbance wavelength and θ is the cell angle with respect to the horizontal. The pressure drop across the interface has been taken to equal $\sigma(2/\delta + 1/R)$, where R is the the interface radius of curvature in the direction parallel to the glass plates. Keep in mind that V is here close to zero immediately following the overturn, except due to some compression of the air layer.

A characteristic velocity can be extracted from the above equation if the surface tension is ignored, to give [17,18]

$$U_{ij}^* = \frac{V(\mu_i - \mu_j)}{\mu_i + \mu_j} + \frac{\delta^2 g \sin(\theta) (\rho_i - \rho_j)}{12(\mu_i + \mu_j)}, \quad (10)$$

where, as above, the first term disappears, as the mean translation velocity of the interface $V \sim 0$ and the equation reduces to a balances between buoyancy and viscous stress, in accordance with the definition of G . For a vertical gap ($\theta = 90^\circ$), this gives $U_{oa}^* = 0.097 \text{ m/s}$. The corresponding velocities for PP1, water and pure glycerin against air are $U_{pa}^* = 26.2 \text{ m/s}$; $U_{wa}^* = 12.7 \text{ m/s}$ and $U_{ga}^* = 0.0127 \text{ m/s}$.

Using these velocities the Reynolds number from Eq. (4) becomes 0.05 for pure glycerin but rises to 2×10^5 for the low-viscosity PP1. The larger number could suggest turbulent motions within the PP1. However, keep in mind that the inertia or added mass will govern the bubble motions before the PP1 reaches this larger velocity, where the viscous stress becomes dominant.

Following the rotation of the Hele-Shaw cell, the unstable primary waves on the interfaces grow in amplitude to form isolated fingers, with majority of wave-crests retreating or growing much slower, by the presence of a larger adjacent fingers that continue to grow, in what is called *shielding*. This nonlinear behavior arises from the flow field created by the large fingers that oppose the smaller ones [18]. As the larger fingers continue to grow, they form undulations on their sides and tend to split. Park and Homsy [5] have related this splitting to a modified capillary number Ca' given by

$$Ca' = \frac{\mu U_{\text{finger}}}{\sigma} \left(\frac{W}{2\delta} \right)^2, \quad (11)$$

where U_{finger} is the finger velocity and W is the total width of the Hele-Shaw cell. It was found that if Ca' is higher than 100, the fingers will split. We will show that our cell is wide enough for minimal wall effects.

A. Speed of eruption

The eruption of the air finger through the high-viscosity glycerin into the low-viscosity PP1 layer, as sketched in Fig. 5, leads to the formation of a rapidly growing hemispheric bubble, of radius $R(t)$ and surface velocity $R'(t)$, where the prime denotes the time-derivative. The driving force is the overpressure Δp , from below the glycerin layer, both from the hydrostatics as well as the compression of the air layer

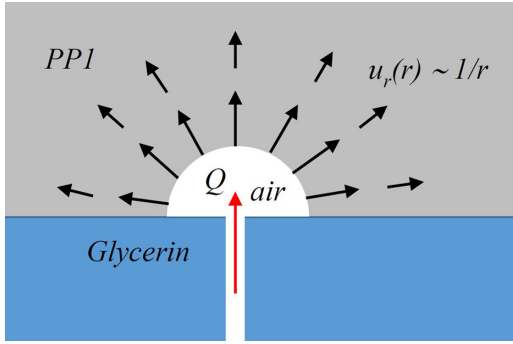


FIG. 5. Setup sketch for the bubble expansion model.

during the early motions, before the finger breaks through. The inertia of the heavy PP1 layer will counteract the radial growth of the bubble. We should also include the potential energy of the displaced liquid, which for a half-circle takes the form $E_{pb} = 4\rho_p\delta gR(t)/(3\pi)$. Considering the low viscosity of the PP1 we formulate the early expansion with an inviscid 2D model. If we assume the overpressure Δp is constant and the motions as purely radial, the velocity is given by continuity,

$$u_r = \frac{Q}{\pi r} = \frac{R'(t)R(t)}{r}.$$

The rate of work done by the pressure, pushing on the cavity wall is $\Delta p u(R(t)) \delta\pi r$ equals the increase in the potential and kinetic energy,

$$E_k = \frac{\delta\rho\pi}{2} \int_{R(t)}^L u_r^2 r dr = \frac{\delta\rho\pi}{2} R'(t)^2 R(t)^2 \ln(L/R).$$

Here we need to limit the domain of integration, as the idealized situation acquires infinite kinetic energy for any movement, as $\ln(\infty/R) = \infty$. Clearly the integration must be cut off considering the total imparted energy, while assuming that L is large enough not to significantly affect the flow next to the interface. Duclaux *et al.* [36] show that $L/R \simeq 2.7$, which we use here. Then we arrive at

$$\pi\delta\Delta p RR' = \frac{d}{dt}(E_k + E_{pb}),$$

giving

$$(R^2)'' + \frac{4g}{3\pi^2} \frac{1}{R} = \frac{\Delta p}{\rho}.$$

If the inertia is more significant than gravity, this relation can be integrated twice,

$$R^2(t) = \frac{\Delta p}{\rho} \left[\frac{1}{2} t^2 + At + B \right]. \quad (12)$$

The integration constants A and B are found by high-speed measurements of an initial radius R_o and edge velocity R'_o . The ratio of potential and kinetic energy $E_{pb}/E_k \sim 1/R R'^2 \sim t^{-1}$. This suggests that the potential energy becomes less important with time from start of the eruption. This could be checked from the actual data. One should also remember that a two-dimensional model ignores any boundary layers on the glass plates owing to the no slip, which will reduce the kinetic energy. Comparison of this model in Eq. (12) with the experimental results can provide an estimate of Δp .

Two other possible resistive forces are surface tension and the viscous tensile stress in the blue glycerin ribbon, stretched above the bubble, which is seen as the blue line above the bubble in Fig. 12. The capillary back-pressure from the surface tension is expressed by $\Delta p = 2\sigma_p/R$, where we use R as the relevant radius of curvature, which then reduces inversely with the growing radius of the bubble. However, using the spacing of the glass plates as the characteristic length, we obtain an upper bound on this pressure by using $R = \delta/2$, to obtain $\Delta p < 10$ Pa. This turns out to be only a small fraction of Δp in Eq. (12). The finger-instability on the top of the bubble (e.g., Fig. 4), also suggests that surface tension along the in-plane curvature has minimal effect here.

The viscous stress in the thin ribbon of glycerin above the bubble, can be thought of as an additional time-varying surface tension, which arises from the axisymmetric viscous stress $\tau = \mu u_r/R^2$. With the thickness of the ribbon δ_r reducing linearly with radius, we readily see that this tension diminishes to typical values around $\tau\delta_r \sim \mu u_r\delta_r/R^2 \sim 10$ Pa, much smaller than the driving force inferred below.

V. RESULTS

A. Overall dynamics

Figure 6 shows a typical sequence of events during the overall dynamics. This we show for a case with all layers of equal depth and using a pure glycerin layer of $\mu_g = 1296$ cP. Immediately following the turn-over the olive oil-air interface, which has the largest density difference of $\Delta\rho_{ao} = 918$ kg/m³, reacts fastest and Rayleigh-Taylor instability quickly forms red fingers traveling down, with large rising air pockets between some of them. This quickly stirs up and overturns these two layers, with the bubbles reaching the oil-glycerin interface, where the larger viscosity slows down their motions and makes them spread sideways. This leaves a thin oil film under the glycerin, which falls down as red streaks in the third panel.

Secondly, the glycerin-air interface becomes unstable with large air fingers rising up through the glycerin layer erupting into the PP1 layer in the seventh panel. The air flows quickly through a few of these air-channels to empty the air layer. These localized air-eruptions are followed by prominent PP1 fingers moving down though the glycerin layer and quickly traversing the oil layer below it, reaching the bottom of the cell in panel 11. In the meantime in the first three panels of the second row of Fig. 6, all four phases briefly interact to form complicated patterns. Finally, the glycerin (blue) and olive oil (red) layers, spanning the center of the cell, slowly overturn to eventually reform the stable-density configuration. We will now describe the various processes in turn.

B. Overturn of air-olive oil layers

The overall timescale of the overturning dynamics can be characterized by the trajectory of the center-of-mass (c.o.m.) of the different layers, as shown in Fig. 7. We start by looking at the fastest overturn, i.e., the air layer and the olive oil (red layer) shown in the first four frames of Fig. 6. The timescale of this overturning, T_{ao} , is measured from the video and roughly estimated by matching the driving force of buoyancy with the

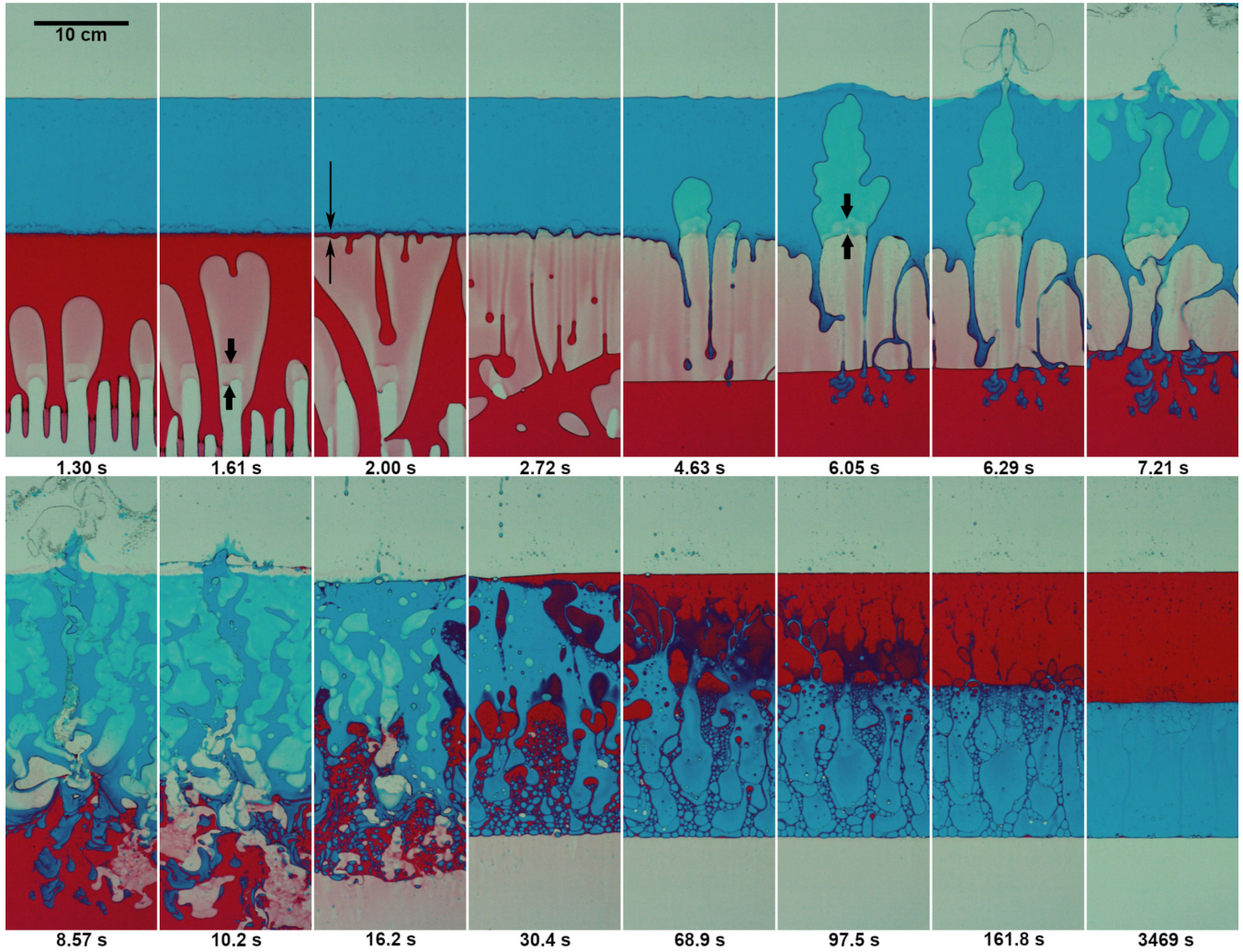


FIG. 6. Snapshots from a full-cell video clip to highlight the overall dynamics after the cell overturn, for pure glycerin and equal layer heights $\Delta H_i = [0.25_a, 0.25_o, 0.25_g, 0.25_p]$. See also the Supplemental Video 1 [47].

inertia and viscous force,

$$T_{ao} \sim L_o/U_{ao}^*,$$

where L_o is the height of the oil layer. The characteristic speed of this process U^* depends in complicated ways on the air-bubble sizes, which in turn is determined initially by the fastest-growing instability at the interface. Keep in mind that only a fraction of the air volume needs to reach the oil-glycerin boundary to start penetrating that interface, but the surface tension and foremost the higher viscosity slows down that process. Using the homogeneous characteristic velocity $U_{ao}^* = 0.097$ m/s from Eq. (10) and the 25 % thick oil layer ($L_o = 0.25 \times 550 = 138$ mm), the timescale of the overturning is therefore $T_{ao} = 1.4$ s, which coincides well with the first minima τ_1 in the curves in Fig. 7(a), for the lower viscosities.

The numerical values of the olive oil minima in c.o.m. reveal another aspect of the dynamics imposed by the viscosity of the glycerin-water layer. The larger μ_g becomes, the lower is the minima in oil c.o.m., reaching the smallest possible value for c.o.m. of $1/8 = 0.125$, while for lower μ_g

c.o.m. reaches only 0.19. This is explained by large viscosity of the glycerin-water layer blocking PP1 or glycerin-water from reaching and entering the oil layer before it has fully interchanged with the air layer. This is seen in the fifth panel of Fig. 6 where the red oil has fully reached the cell bottom before the blue fingers of glycerin enter it in the sixth panel. Subsequently, the two heavier layers of PP1 and glycerin gradually lift the c.o.m. of the oil toward its equilibrium position of $5/8 = 0.625$, after a timescale of minutes, based on extrapolation of Fig. 7(a).

The c.o.m. for the water-glycerin layer shows a more complicated evolution with a maximum, marked by τ_2 , following the first minimum τ_1 , as discussed in a following subsection.

The first Rayleigh-Taylor instability at the olive oil-air interface grows so rapidly, that it starts during the overturning of the cell, which typically only takes 1–2 s. The wavelength of undulations, like those shown in Fig. 8(a), was measured in a number of experimental runs, showing an average $\lambda = 22.5 \pm 0.9$ mm, which is near the predicted fastest growing wavelength in Eq. (9) $\lambda_{ao}^* = 20$ mm. In a later section with only three fluid layers, Fig. 29 shows a larger

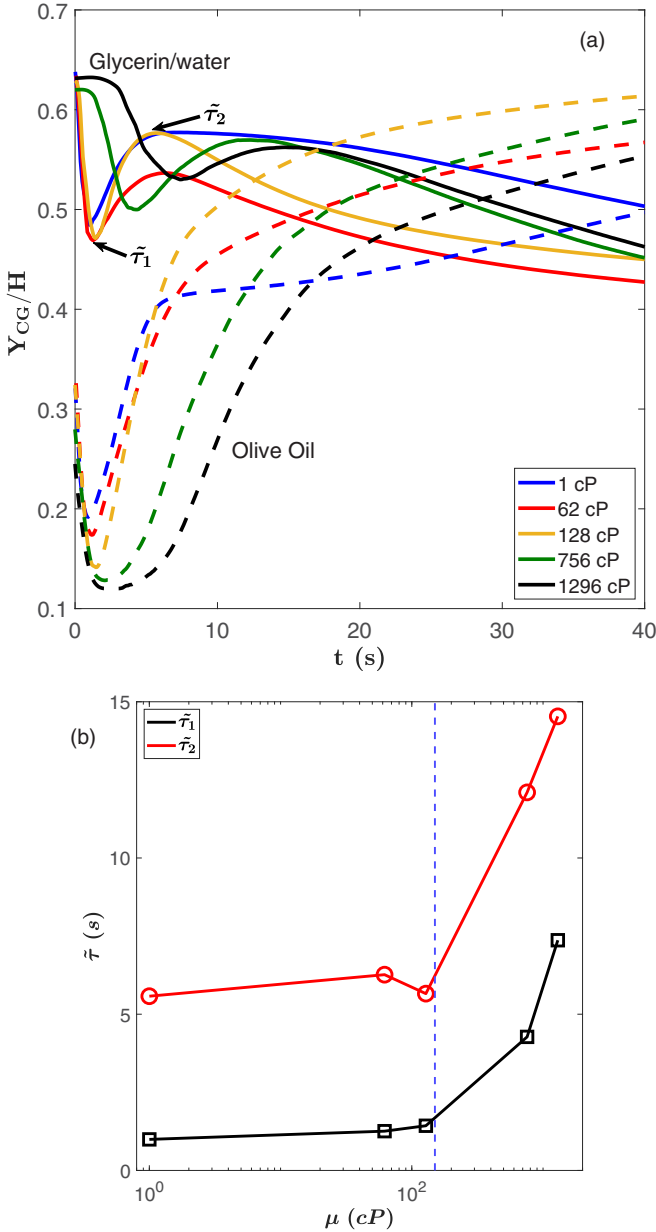


FIG. 7. (a) Time-evolution of the center-of-mass of the glycerin-water layer (solid lines), over a range of different viscosities. The dashed lines show the corresponding center-of-mass for the olive oil layer. These realizations are for cases where all the layers have the same thickness $\Delta H_i = [0.25_a, 0.25_o, 0.25_{g/w}, 0.25_p]$. (b) The time it takes to reach the early minimum and maximum in the center-of-mass locations of the glycerin-water layer, as marked by the arrows in panel (a). The vertical dashed line is simply to aid the eye to see where the viscous effects start increasing these timescales.

wavelength for pure-glycerin-air interface of $\lambda_{ga} = 28.6$ mm which again compares reasonably well with $\lambda_{ga}^* = 25$ mm from the theory. Both wavelengths are slightly longer than predicted. Figure 29 also highlights the much faster growth-rate on the glycerin-air ($\alpha^* = 41$ s⁻¹) than the PP1-glycerin interface ($\alpha^* = 12.7$ s⁻¹), with the bottom instability overtaking the dynamics before the top one can even start significant development.

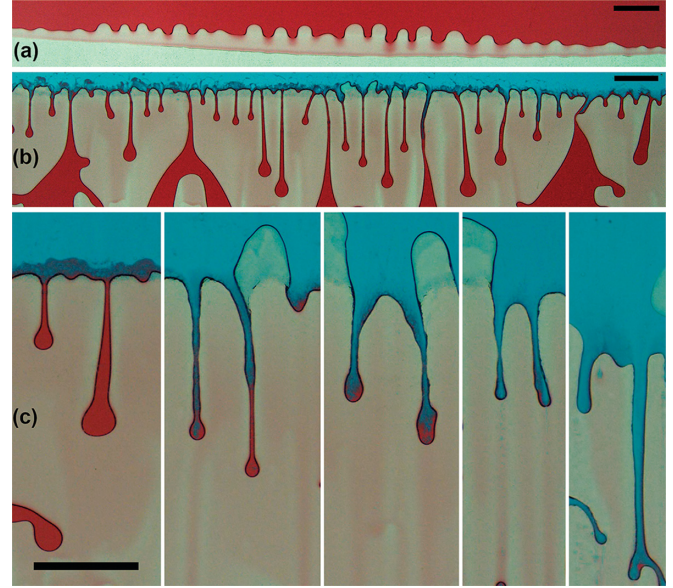


FIG. 8. (a) The earliest instability of the olive oil-air interface, with undulations starting before the overturn is complete. (b) Fingers from the olive oil film remaining under the glycerin, as the air pockets expand horizontally. (c) Glycerin finger tips covered by the red olive oil. The red wetting layer becomes thinner as more generations of fingers have emerged. For $\Delta H_i = [0.35_a, 0.25_o, 0.25_g, 0.15_p]$. All scale bars are 50 μ m long. See also Supplemental Video 1 [47].

1. Wetting and contact-lines

The presence of contact lines can slow down the speed of air fingers, as was highlighted by Kopf-Sill and Homsy [37]. Surfactants can also slow down these motions [10,38,39], but are completely absent in our setup.

The second panel in Fig. 6, shows two superimposed contact lines in the color profiles, at the base region of the air fingers entering the red oil layer. In other words, the air fingers have thin oil-films along the glass surfaces, with air-oil-glass contact lines, which are slightly shifted in the vertical direction, showing clear jumps in the intensity of the red color, marked by arrows in the second panel of Fig. 6. The overturning of the cell may promote this shift. Measuring the thickness of these liquid films is beyond the scope of the current study, but has been investigated extensively [12,40].

At a few locations along the original interface, fingers of blue glycerin start forming on top of the red oil. This instability is driven by a much smaller density difference $\Delta\rho_{og} = 0.311$ g/cm³ than between the air and glycerin $\Delta\rho_{ag} = 1.23$ g/cm³ and the growth of those fingers is too slow to affect the overall dynamics.

Figure 6 (third panel) and 8(b) show a second characteristic phenomenon where the air-pocket approaching the oil-glycerin interface expands horizontally before it can penetrating into the glycerin, thereby leaving a film of oil being squeezed between the two fluid layers. This oil film is of typical thickness $\simeq 5$ μ m, as marked by arrows in the third panel in Fig. 6. If this film is thick enough it will lead to a second formation of oil fingers which fall into the air pockets. The following glycerin fingers have red tips, as shown in the close-up images in Fig. 8(c). This figure shows that

subsequent generations of fingers also retain some red color olive oil coating on their surface. This persistence of a red oil layer coating film can be explained by the *spreading parameter*, which characterizes the propensity of a liquid lens to being pulled by surface tension to cover a liquid-gas interface. It is defined as [41]

$$S = \sigma_{ag} - \sigma_{og} - \sigma_{ao} = 23 \text{ mN/m} \gg 0.$$

Here, the large positive value for S shows that the balance of the three surface tensions meeting at the oil-glycerin-air triple line will pull the oil onto the glycerin-air interface, as is indeed observed [41,42]. If the layer ruptures, this balance will close it again. This continues until all the olive oil has been swept from the interface by the falling fingers and pure blue fingers are observed to fall into the air layer.

Furthermore, when the air fingers penetrate into the blue glycerin a pair of new contact lines appear, see arrows in Fig. 6 (sixth panel). Here arises an additional complication, i.e., there remains a thin olive oil film on the glass and the air does likely not touch the glass, but pulls some of this oil-film into the glycerin, giving rise to a contact line between oil-glycerin-glass and a second triple-line between air-oil-glycerin.

Finally, when the air fingers reach the top of the glycerin layer they erupt rapidly into the PP1 layer, the phenomenon which is the main focus of this study.

2. Effect of viscosity

The viscosity of the glycerin-water mixture was systematically varied over a large range, by using different glycerin concentrations, as listed in Table I and indicated in Fig. 3(b). The most important effect of higher viscosity is to delay the penetration of the air fingers through this layer allowing the air to collect under it, on top of the oil layer. Therefore, the PP1 fingers which make it through the glycerin layer from the top can fall through its bottom glycerin-air interface, entering into free-fall through the air layer before the glycerin-water has moved down to the top of the olive oil (e.g., Fig. 22).

The overall settling behavior of the glycerin-water layer can be investigated by considering its c.o.m.. After the cell overturned, all the liquid layers will eventually move downward by the action of gravity. However, the detailed dynamics are complicated by the interaction of the individual layers. As can be observed by the plots in Fig. 7(a) the c.o.m. curves for the glycerin are all qualitatively similar, with an initial downward motion, reaching a local minimum, marked by time τ_1 , as this liquid replaces the air. However, for the two most viscous glycerin-water layers reaching this minimum takes much longer than for the oil layer. For the pure glycerin, the height of the c.o.m. remains constant for the first 3 s. Following this, after the air eruptions, the c.o.m. rises again, due to the rapid decent of the PP1 through both the glycerin-water and the olive oil. This forms a local maxima at τ_2 . Finally, the glycerin-water c.o.m. resumes its downward motion by exchanging location with the oil layer, over a timescale of about a minute.

Figure 7(b) shows the changes in the timescales τ_1 and τ_2 as the viscosity μ_g is varied over the full range of values. The time-scale values show that below $\mu_g \sim 150$ cP this viscosity

TABLE III. Darcy-Rayleigh numbers G for the fingers in different glycerin-water concentrations.

Mixture	μ_g cP	ρ_g kg/m ³	U m/s	G
Pure water	0.97	998	0.621	21.2
65 % glycerin	62	1181	0.566	0.440
80 % glycerin	128	1217	0.368	0.338
95 % glycerin	570	1251	0.115	0.249
96.7 % glycerin	756	1254	0.0692	0.313
100 % glycerin	1296	1260	0.0385	0.330

is not the controlling parameter. This coincides approximately with the viscosity of the oil layer.

3. Air-finger velocity

Immediately following the rotation of the cell, broad air fingers start rising through the oil layer toward the interface with the glycerin-water layer, as in the first panel in Fig. 6. How these fingers traverse this interface, depends primarily on the viscosity of the glycerin-water layer. Subsequently, isolated fingers move through the glycerin-water layer, see e.g., panel 5 in Fig. 6. Figures 9(a) and 9(b) track the tips of typical fingers moving through the olive oil in Fig. 9(b) and then through the glycerin-water in Fig. 9(a). This is shown over the range of glycerin-water concentrations with viscosity μ_g , the value of which determines the interaction of the finger with the interface, as is depicted in Fig. 10. Figure 9(c) shows the rise velocity of the tip of the fingers. For $\mu_g > 100$ cP this velocity decreases linearly with μ_g , while below 100 cP the viscosity is too weak to govern the motions when reaching the interface.

By tracking the tip of the air finger while it penetrates the glycerin-water layer, several observations can be made based upon the plots in Fig. 9.

Three general behaviours are observed, as shown in Fig. 10. The first case is when the glycerin-water layer viscosity is very low. The quickest air fingers that pass through the oil layer will penetrate the oil-glycerin-water interface without slowing down. Also, these fingers will balloon up after that accumulating into a very wide eruption as they pass into the PP1 layer. The low viscosity of the water-glycerin layer causes the interface between it and the PP1 layer to quickly become very unstable after overturning the cell. This interface instability manifests itself in a formation of a shape that resembles a mushroom.

The second case is when the viscosity of the glycerin-water layer is close to the same as that of the oil. In this case the air fingers that infiltrate the oil will continue to grow through the glycerin layer almost at the same rate. This continuous growth tends as well to create a wide spread eruption when the air reaches the PP1 layer, unless the finger splits before reaching the PP1 layer.

The third case is when the glycerin layer is pure and has a very high viscosity of $\mu_g = 1296$ cP. In this case, the air has completely overturned the oil layer before it start to penetrate the glycerin, through new instability and finger formation, as shown in Fig. 6 and is the focus of our study.

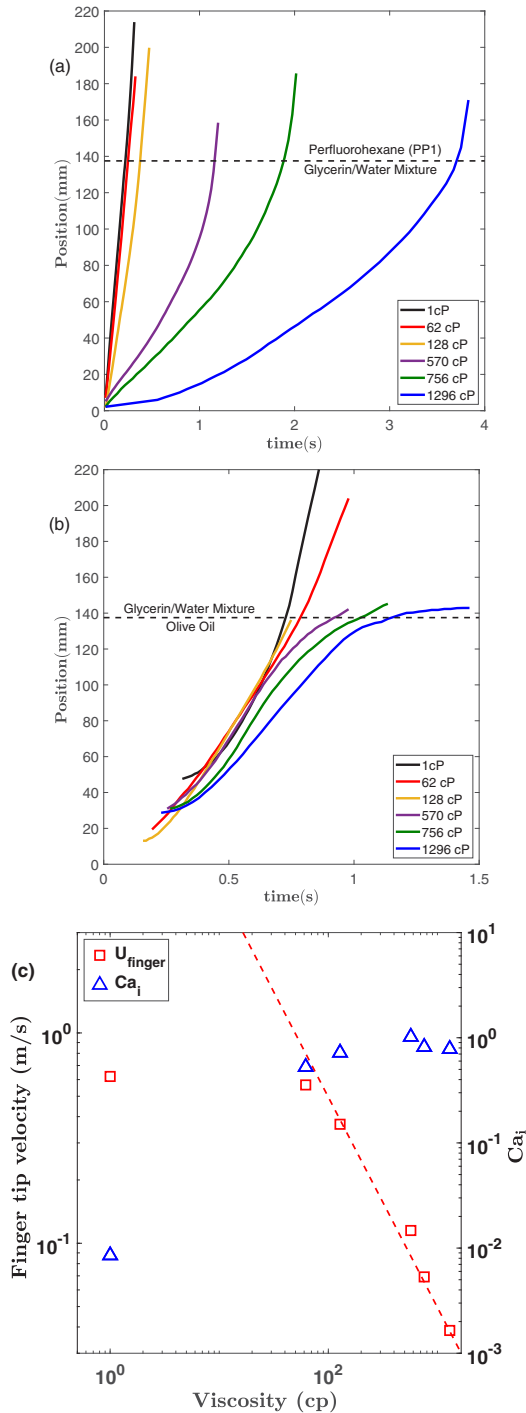


FIG. 9. Vertical motion of the air-finger tip during its penetration of the glycerin-water layer (a) and the olive oil layer (b), for different viscosities μ_g of the glycerin-water layer, while all layer are of equal depth, i.e., 25 %, which corresponds to 137.5 mm. The dashed line represent the original location of the the interface between the glycerin-water layer and olive oil or PP1 layer, while the reference zero position is set at the bottom of the lower layer. (c) The average tip velocity within the glycerin-water layer, before the finger hits the PP1 interface vs its viscosity μ_g . The dashed line has a slope of -1 . The right abscissa shows the corresponding value of the capillary number Ca_g from Eq. (7).

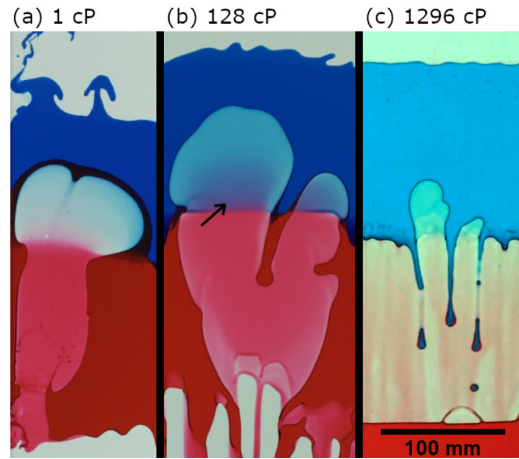


FIG. 10. The influence of the viscosity of the glycerin-water layer, on the air-finger growth. (a) Finger for the water only case ($\mu_g = 1$ cP). (b) The case of glycerin-water layer with similar viscosity as the oil layer ($\mu_g \approx 128$ cP). (c) Start of a finger for pure glycerin ($\mu_g = 1296$ cP). The corresponding Darcy-Rayleigh number G [Eq. (5)], using the speed of the fingers, are given in Table III.

The interface instability on top of the glycerin-water layer at the interface with the PP1 grows much more slowly. Consequently, if the glycerin-water layer is not very thick, the first air finger will penetrate through the layer before this instability has a time to develop significantly. After the first eruption this interface instability will grow rapidly, as will be shown in Fig. 21. By contrast, as the glycerin-water layer viscosity increases, the air-finger displacement will follow a parabolic behavior at a lower velocity. Second, if the glycerin-water layer viscosity is large enough, the tip will experience a rapid acceleration as it approach the top interface between glycerin-water and the PP1 layer, due to the reduction in effective viscosity from the fractional area of glycerin surrounding the air finger. This rapid acceleration phenomena will be addressed in subsection C of the Results.

As mentioned above Fig. 9(c) shows the finger-tip velocity versus μ_g , showing an inverse relation between speed and viscosity, until viscosity reduces below ~ 80 cP, where inertia starts playing a dominant role, slowing down the motions, beyond what would be expected if only viscosity were counteracting them. This corresponds the $Re_i \approx 33$ in Eq. (4). This transition occurs for μ_g of the same order as in Fig. 7(b) for the overall motions. The slow-down with viscosity follows the same power-law scaling as predicted in Eq. (10), i.e., $U \sim \mu^{-1}$, as the density and viscosity of the air is insignificant. However, the prefactor is larger by ~ 3 . However, these are average velocities which vary somewhat during their rise in Fig. 9(a).

4. Effect of relative layer thicknesses

We have systematically varied the thicknesses of the air, PP1, and glycerin layers, while keeping the olive oil thickness constant at 25 %. The experimental results (Fig. 15 and 17) will show that the layer thicknesses are not as important as

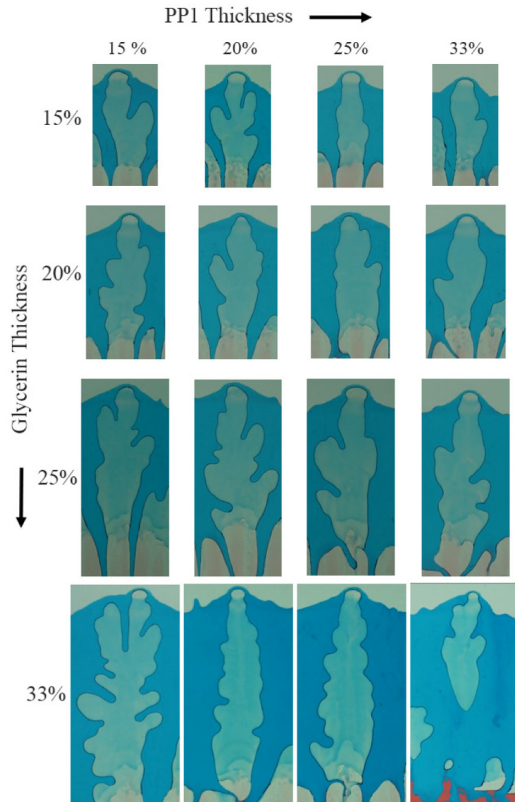


FIG. 11. The changes in the typical shapes of the air fingers, rising through the pure glycerin layer (blue), as they are about to erupt into the top PP1 layer. Shown for the full range of different layer thicknesses. The thickness of the glycerin layer increases from top to bottom, whereas the thickness of the PP1 layer (transparent layer on top of the glycerin layer) is gradually increased from left to right. Only for the thickest PP1+glycerin layer vertical depths does the air finger pinch off at its base, owing to the very small height of the air layer of 9%.

the viscosity of the glycerin-water layer μ_g , which is changed over a much larger range of values. The strongest effect of the layer thicknesses relates to the overall potential energy impacted on the fluid stack when it is overturned. The thickness of the air layer has the biggest effect on this, but can also control the length of the air fingers.

Increasing the thicknesses of the liquid layers will allow the air fingers to evolve over a longer distance, which typically makes them more susceptible to branching and splitting, as is clear in Fig. 11.

However, by increasing the thicknesses of the liquid layers, this limits the depth of the air layer. If the air layer thickness is small enough the air fingers can be pinched off at their base, becoming engulfed by the liquid layers. This in turn will cause the air to travel as separated bubbles, as can be seen in the lower-right corner of Fig. 11. This pinch-off stops the rapid channeling of air through the viscous layer.

The relative thickness of air and PP1 also leads to significant effects. For example when the PP1 layer is small the rising air can quickly fill it and then follow the PP1

downward through channels, as will be shown in a later section.

C. Eruptions of air pockets

The strongest buoyancy forces occur when the air-bubbles enter into the densest liquid layer, i.e., into the perfluorohexane (PP1). This occurs after the air-bubbles have transited both the oil layer and the water-glycerin layer. When the air finger enters the low-viscosity PP1 it expands rapidly to form a hemispheric bubble. This is shown in Figs. 4, 6, and a closeup in Fig. 12. The location of the first eruption is often near the center of the cell but usually occurs at a few locations along the horizontal interface, at different times, as the first eruption suppresses the other fingers. The rapid dynamics require close-up imaging with the high-speed video camera, which has a reduced number of pixels and can only record a limited region along the interface while retaining a sufficient spatial resolution. By focusing at the center we can capture these eruptions by trial and error. The air finger penetrates into the heavy PP1 layer through a narrow neck in the blue glycerin, which in the first frame of Fig. 12 is $\simeq 2$ cm wide. The neck contracts and pinches off in the seventh panel of Fig. 12. This pinch-off and air eruptions occur repeatedly, as shown in Supplemental Video 2 [47].

The top boundary of the air-bubble retains a thin ribbon of blue glycerin that proceeds to be stretched into a half-circle. Figure 13 tracks this thinning of the ribbon over 77 ms, spanning the first four panels in Fig. 12, with the in-plane thickness reducing by a factor of 4, from 6 to 1.5 mm. When the glycerin ribbon becomes significantly thinner than the channel width $\delta = 3.9$ mm the air will typically bypass it, as explained in the sketch in Fig. 14(b). Later on this viscous ribbon folds and buckles into complex shapes in the middle row of Fig. 12, before breaking into smaller pieces in the last row. The flow around the inlet pulls up the base of the thread starting in the fifth panel to form a mushroom shape.

The speed of the airflow into this mushroom shape can be measured from the sequence of video frames in two ways: first from the growth in area of the bubble and secondly by following the small spray droplets. Figure 15 shows the change in area and thereby the velocity through the neck. The area growth-rate, i.e., the volume flow-rate, increases with time.

As the first air pocket passes from the glycerin-water layer into the PP1 layer, two thin films remain on each glass plate, i.e., a PP1 layer wetting the surface and a thin glycerin-water film between it and the air. Almost immediately this blue film ruptures on both sides of the air finger, as seen in Fig. 14(a). These multiple lighter-colored spots expand rapidly. The rate of this expansion is captured in the video and can be used to roughly estimate the film thickness, based on a modified Taylor-Culick law:

$$u_{\text{edge}} = \sqrt{\frac{2\sigma^*}{\rho \delta_{\text{film}}}}, \quad (13)$$

where u_{edge} is the velocity of the boundary of the ruptures, which is expected to be a constant. Here σ^* needs to be selected as the net driving surface tension, accounting for the

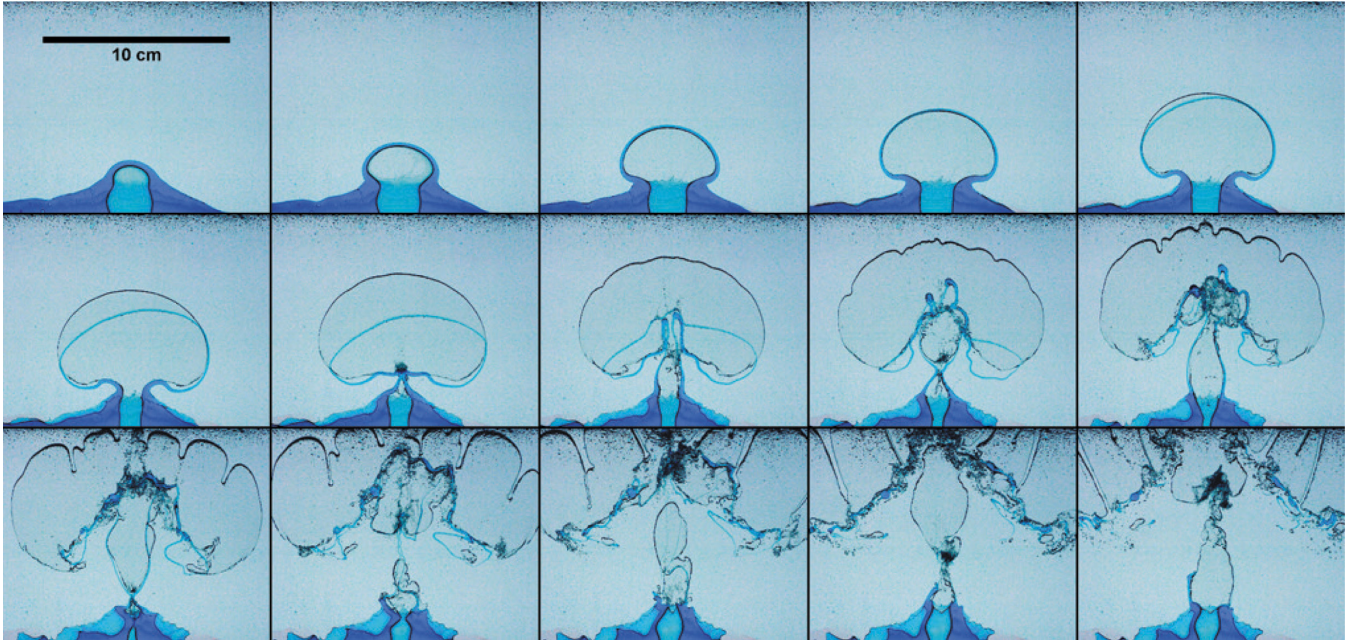


FIG. 12. Example of an air-bubble eruption through the blue glycerin-water layer into the PP1 layer. The frames are spaced by 24 ms. Here we use pure glycerin and the layer thicknesses are $\Delta H_i = [0.25_a, 0.25_o, 0.25_g, 0.25_p]$. See also online Supplemental Video 2 [47].

balance at the triple line between the two immiscible liquids and the air, which is here estimated as $\sigma^* = (\sigma_{pg} + \sigma_{ga} - \sigma_{pa})/2 = 51 \text{ dyn/cm}$ [42]. The measured speeds are $u_{\text{edge}} \sim 0.8 \text{ m/s}$, which corresponds to film thicknesses of $\delta_{\text{film}} \simeq 140 \text{ }\mu\text{m}$. The dewetting rate is also influenced by the viscosity of the film as have been previously established by Reysat and Quéré [43]. Large density differences have recently been studied by Jian *et al.* [44]. This rupture process still leaves a wetting film of PP1 on the glass plates, as becomes clear

from the subsequent dynamics by the appearance of waves and spray formation by the airflow.

1. Comparison with inertia modeling

Figure 15 compares the growth-rate of the erupting bubble with the model developed in Sec. IV A, through Eq. (12). The initial values of R_o and R'_o are measured at the earliest stage of the curves and Δp is obtained by fitting to the subsequent evolution. The shape of the fits to the data are excellent for both of the largest viscosities in Figs 15(a) and 15(b). The assumption of the model is that Δp is constant during the rapid expansion, deriving the overpressure by the depth of the liquid layers pushing on the air layer at the base of the fingers. Figure 15(c) demonstrates that the best-fit pressures increase with larger combined height of the two liquid layers, consistent with the above assumption. However, even though the trends in Δp are consistent, the magnitudes are much lower, i.e., $\rho_g g H_{25\%} \simeq 1400 \text{ Pa}$. This can be explained by two subtle effects: First our cell is completely closed from the surroundings, which will produce suction pressure from the top to counteract gravity and reduce the compression of the air layer, if one ignores the small deformations of the glass walls. Once the air-channel opens through the glycerin layer, the release of pressure induces a sudden downward motion of the glycerin layer (see Fig. 21) which adds viscous stress to counteract the sustained back pressure. Second, there is some pressure drop in the airflow through the narrow channel, which reduces the effective Δp at the base of the growing bubble.

Future experiments where the top of the PP1 layer is opened to the atmosphere after the turn-over, should show faster bubble growth, but this is beyond the capabilities of the current setup.

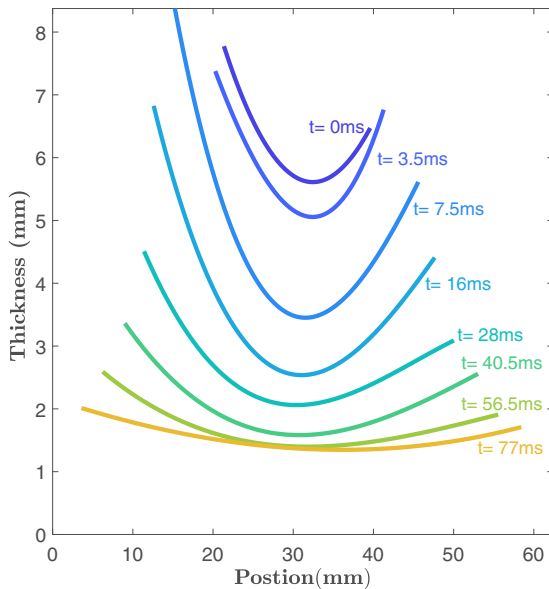


FIG. 13. The thinning of the glycerin ribbon above the air bubble along the interface vs time, as the air-finger front erupts trough the interface into the PP1 layer above it. For the case of a pure glycerin layer of $\mu_g = 1296 \text{ cP}$ and with all the layers having the same 25 % thickness.

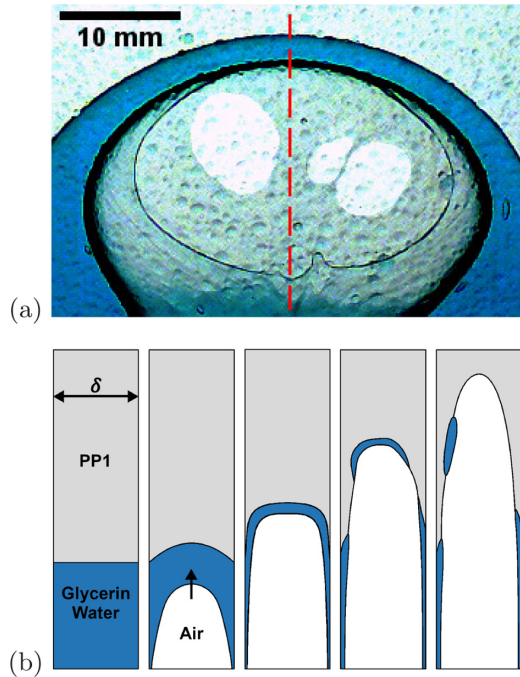


FIG. 14. (a) Close-up image of the air finger at the start of the eruption, when it passes up through the top of the blue glycerin-water into the PP1 layer. This leaves two thin glycerin films on top of the PP1 layers on the glass plates, as sketched in the cross-sectional view in (b). These blue glycerin films rupture to allow the air to come in contact with the lower surface-energy PP1 films along the glass. The darker outline corresponds to the *dewetting* spot on the front glass plate, whereas the three brighter spots are next to the back plate. The image contrast has been enhanced to allow for better visibility. Realization is for pure glycerin and $\Delta H_i = [0.25_a, 0.25_o, 0.25_g, 0.25_p]$ (b) Sketch of the liquid interfaces and film breakup in a plane perpendicular to the glass, i.e., in the plane marked by the red dashed line in (a). Shows how the air penetrates past the glycerin filament, as is clear starting from the fifth panel of Fig. 12.

2. Spray droplets

Following the bubble eruption and the release of the pressure, the neck becomes narrower starting in the third panel and pinches off in the seventh panel of Fig. 12. The driving force for this necking is likely a combination of horizontal hydrostatic pressure and Bernoulli or venturi pressure, owing to the strong airflow velocity in the neck. When the necking occurs high in the channel where the glycerin film has already ruptured, i.e., above the light-blue neck area in panel 6 of Fig. 12, the fast airflow can destabilize the low-viscosity PP1 film on the glass, leading to the ejection of a large number of PP1 droplets. These droplets appear as dark clouds due to the large number of refractive interfaces, as is shown in the fourth and fifth panels of Fig. 16. This is also seen in subsequent pinch-offs in panels 11 and 15 of Fig. 16. The close-up high-speed video allows us to determine the speed of the fine spray droplets, as plotted in Fig. 17. Typically, a few tiny droplets first emerge at higher speed, before the dark cloud of the myriad of the fine droplets appears. Both of these velocities are presented in the figure averaged over numerous realizations. The details of the necking differ between erup-

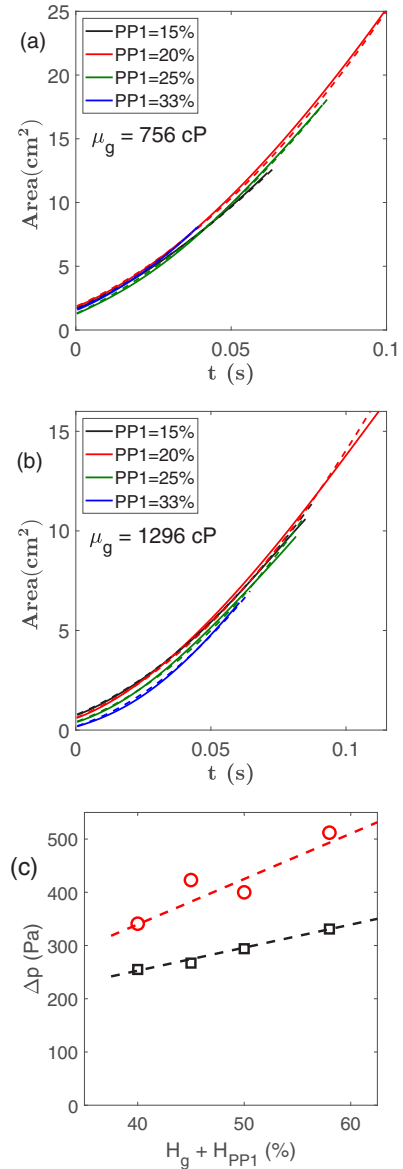


FIG. 15. The expansion rate of the bubble area during the air eruption at fixed glycerin-water-layer thickness, but for different PP1 layer thicknesses. The solid curves are from the video data, while the dashed curves are the best fits using the model in Eq. (12), using Δp as the fitting parameter. (a) The glycerine-water layer viscosity of $\mu_g = 756$ cP. (b) Pure glycerine layer with $\mu_g = 1296$ cP. (c) The best-fit pressures Δp for each curve in (a) red circles and in (b) black squares.

tions, based on neck shape, depth of the pinch-off, angle of the finger, etc. This results in a large range of values, with no clear difference between the two glycerin-water viscosities, with only a weak increase in ejected velocities with larger depth of the glycerin-water and PP1 liquid layers. This is most likely arising from the larger driving pressures Δp as in Fig. 15(c).

Different behavior occurs if the pinch-off takes place inside the glycerin, as shown in Fig. 18.

Figure 17 shows that the average velocity of the cloud of droplets ranges between 1.5 to 2.0 m/s, while the fastest initial droplets can reach velocities between 2.5 to 4 m/s. As these droplets rise up through the air cavity, they

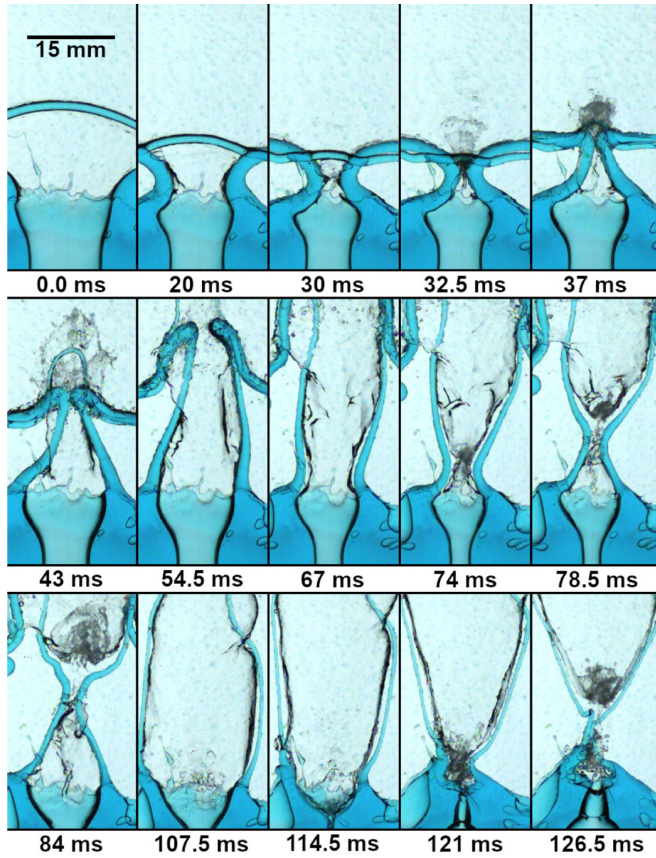


FIG. 16. Close-up imaging of the neck pinching and droplet spraying that occurs after the air finger erupts from the pure glycerin layer into the PP1 layer, for $\Delta H_i = [0.17_a, 0.25_o, 0.25_g, 0.33_p]$. The first three neck pinch-offs and spraying are shown, one in each row. See also Supplemental Video 3 [47].

tend to coalesce back with thin PP1 layers that remain on the glass plates, or impact the ceiling of the bubble. The air speed through the neck can be calculated from the expansion of the bubble area in Fig. 15(a), giving increasing speeds with time, from 0.7 to 1.7 m/s in this figure, using a neck-width of 2 cm. The appearance of the droplets only for a narrower neck is therefore consistent with the air speed needing to be larger than the droplets it drives. The high-speed video corresponding to Fig. 16 shows the first clear droplets emerge when the neck-width is about 2.5 mm, suggesting air speeds ~ 20 m/s in the restricted channel. The Supplemental Video 3 [47] shows waves on the PP1 film as well as the ejected droplets.

Having an estimate for the air velocity we can look at the relative strength of the hydrostatic and venturi pressures, during the air-cylinder pinch-off. We do this by taking the ratio of these pressures:

$$\gamma = \frac{1}{2} \rho_{\text{air}} U_{\text{air}}^2 / (\rho_p g H_p),$$

which changes with time, as the thickness H_p of the PP1 layer reduces. The air speed also changes greatly with neck width. Using half the original value of H_p , we see γ increase from 0.003 to 0.34, showing that hydrostatics dominate, while venturi effects will accelerate the closing of the neck only during the final stage of the pinch-off. Figure 19 shows this ac-

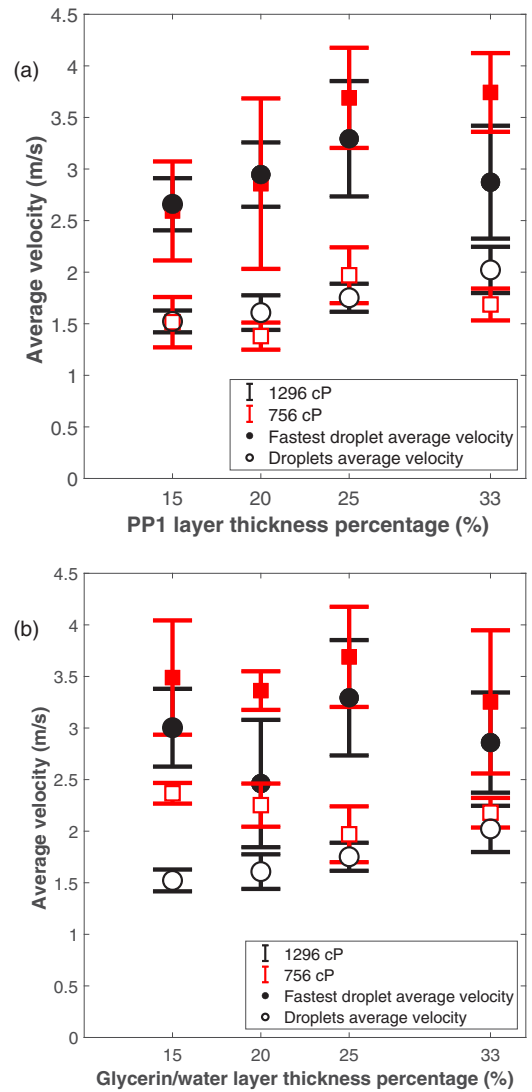


FIG. 17. The average velocity of the droplet clouds ejected during many neck pinch-offs. The error bars highlight the range of average velocities for many realizations, each averaged over 4–6 neck pinch-offs. Results for two different glycerin-water viscosities. (a) The thickness of the glycerin-water layer is kept at a quarter of the cell height, while the PP1-layer thickness is varied. (b) The thickness of the PP1 layer is kept at a quarter of the cell height, while the glycerin-water-layer thickness is varied.

celeration near the final pinch-off. The larger viscosity closes slower, but also accelerates at the end.

If the pinch-off occurs further down from the top of the glycerin layer, where the walls of the air-tube are still fully made of glycerin-water, the continuing airflow can blow up a viscous bag, as is shown in the sequences in Fig. 18. These thin-walled viscous bags are stretched until the films rupture at numerous locations, starting in panel 5 in Fig. 18(b), leaving many minuscule droplets. Based on the Taylor-Culick velocity of the rupture speed of 17 m/s, these films are only $\sim 0.4 \mu\text{m}$ thick.

The narrow air jet can also propel the blue glycerin filaments above the neck into the bubble, as in the close-up sequence in Fig. 16.

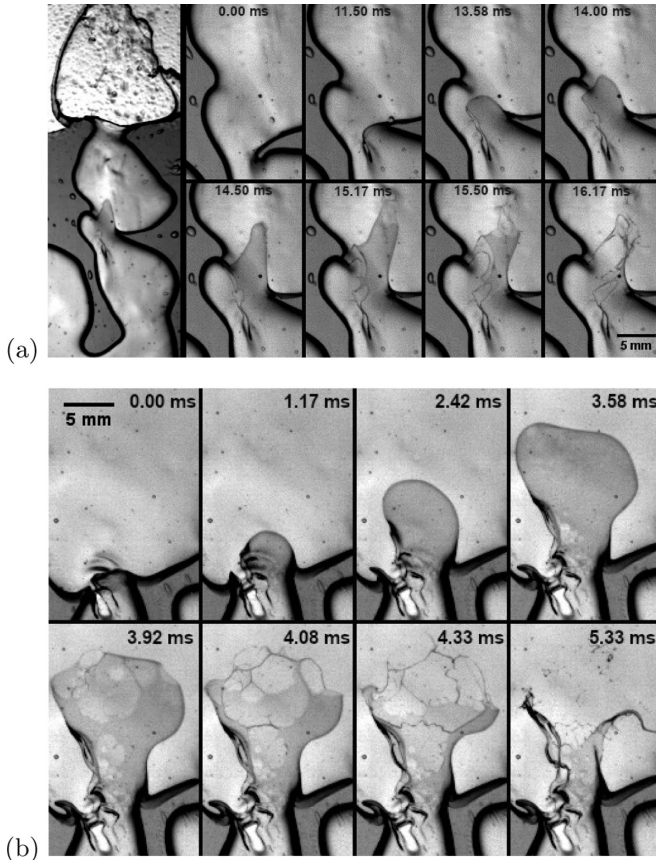


FIG. 18. The formation of glycerin bags, when the air-channel pinches off below the PP1 layer, inside the glycerin. (a) The formation of the pocket in a narrow passage within the glycerin-water layer. (b) Close-up of the expansion and breakup of a glycerin pocket. Both sequences are for $\Delta H_i = [0.35_a, 0.25_a, 0.20_{97\%g}, 0.20_p]$. See also Supplemental Videos 4 and 5 [47].

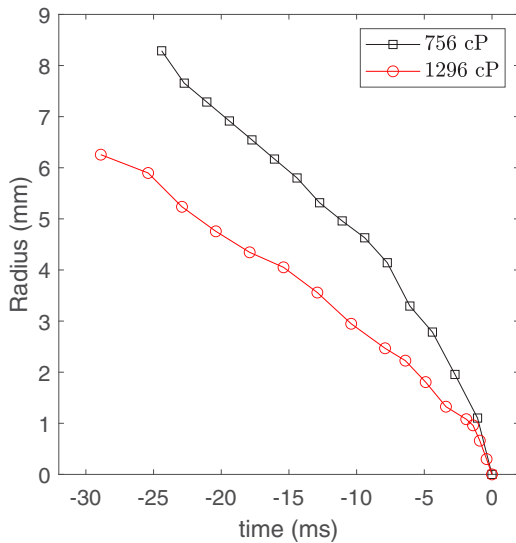


FIG. 19. Pinch-off radius of the neck vs time, for the first pinch-offs, like those in Figs. 12 and 23. For two different viscosities. Subsequent pinch-offs become more irregular, as is clear from the Supplemental Video 2 [47].

TABLE IV. Number of neck pinch-offs for two different viscosities of the glycerin-water layer μ_g and a range of different thicknesses of the air layer. The “+” sign indicates lower bounds, as the count is limited by the finite length of the high-speed video clips.

μ_g	17 % H_{air}	25 % H_{air}	30 % H_{air}	35 % H_{air}
756 cP	3	8	7	11
1296 cP	6	10	10+	13+

3. Pinch-off frequency

Following the first pinch-off the channel opens again and pinches off repeatedly, as is seen in the Supplemental Videos 2 and 3 [47]. The total number of pinch-offs are listed in Table IV. This phenomenon continues while the channel remains

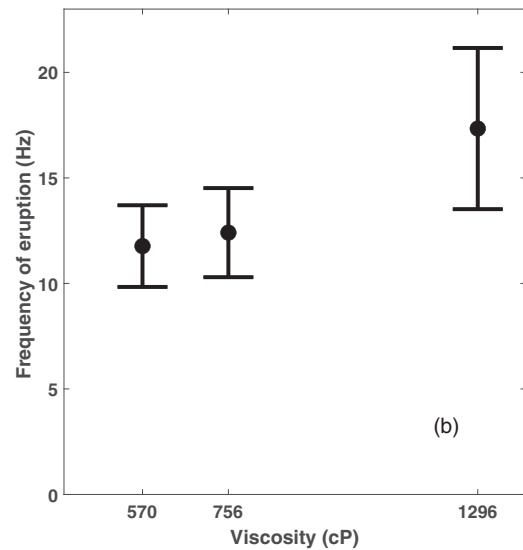
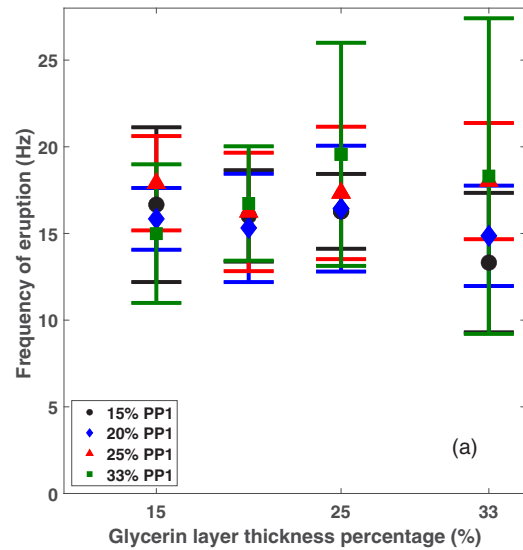


FIG. 20. The frequency of the neck-pinching during the eruption of the main finger. (a) Pinch-off frequency for different thicknesses of pure glycerin and PP1 layers, with $\mu_g = 1296$ cP. (b) The influence of the viscosity of the blue glycerin-water layer on the pinch-off frequency, for the case where all the layers have the same thickness.

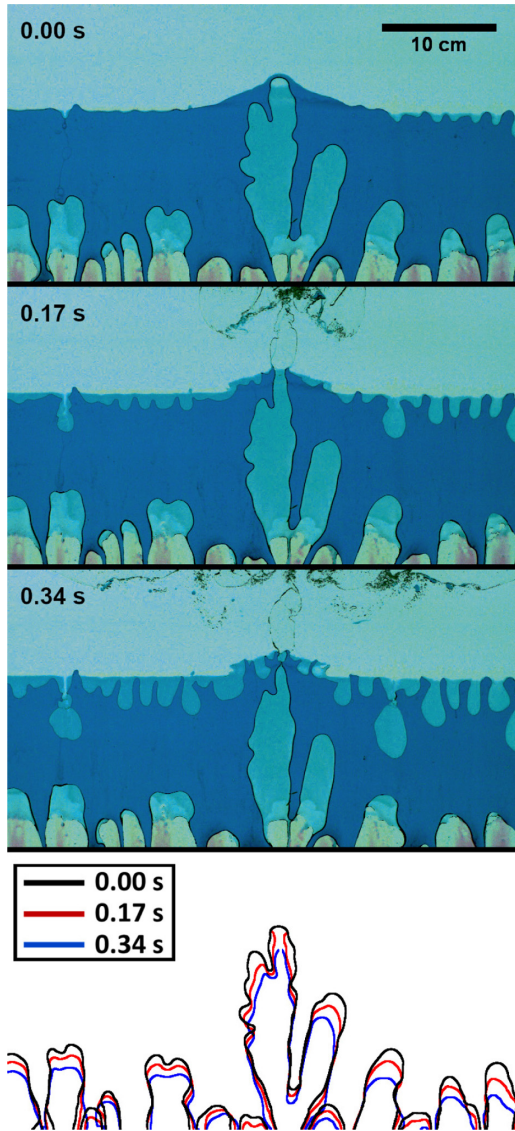


FIG. 21. The downward motion of the tips of the air fingers following the eruption of the first air finger through the top of the glycerin-water layer, for $\Delta H_i = [0.25_a, 0.25_o, 0.25_g, 0.25_p]$. The bottom sketch superimposes the traces of the air-glycerin interfaces. The frames are separated from each other by 0.17 s. Note that the tips of the air fingers move downward against buoyancy. See also Supplemental Video 1 [47].

intact and there is air left. Therefore, the largest numbers are for the thickest air layers, i.e., smallest PP1 layers. The larger viscosity μ_g also shows significantly larger number of pinch-offs.

Figure 20(a) shows that the frequency of pinch-offs is around 15 Hz, but varies over a wide range. This suggests local dynamics, which in turn are sensitive to the shape of the air channel, which is subject to the random splitting and side-branching of the original air finger, even though the overall dynamics are qualitatively similar, as seen in Fig. 11. Figure 20(b) investigates the effect of the glycerin-water viscosity on the pinch-off frequency, showing slightly lower frequency as the viscosity is reduced, with the average reducing to 12 Hz.

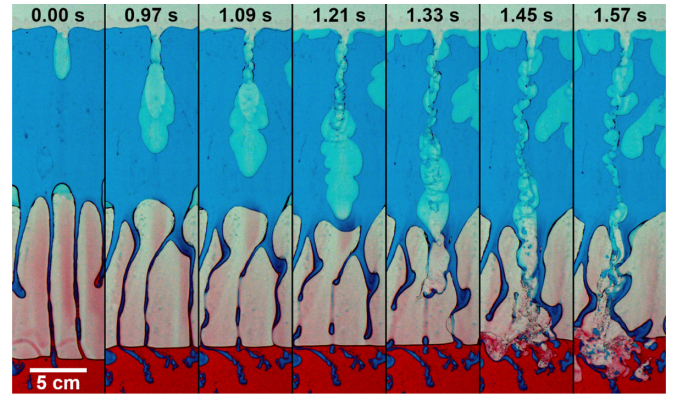


FIG. 22. The penetration of the PP1 phase into the other layers after the initial pinch-off for pure glycerin and equal layer depths: $\Delta H_i = [0.25_a, 0.25_o, 0.25_g, 0.25_p]$.

During the early stage of the motion the weight of the glycerin-water layer compresses the below air layer. This over-pressure is released when the first air fingers break through the glycerin layer and erupts into the PP1 layer. This is most clearly demonstrated in Fig. 21 which traces the outline of the lower air-glycerin interface. It shows the tips of all the other fingers suddenly retreating downward at approximately a constant rate. This behavior is consistent with a sudden release of the air pressure by the channeling through the air finger. This also accelerates the downward motion of the PP1 fingers at the top interface. Supplemental Video 14 [47] shows a striking example of this dynamic for a three-layer system. Keep in mind that continuity and the fixed volume inside the entire cell, also implies suction pressure at the top inside the heavy PP1 layer, immediately following the overturn. The air breakthrough therefore also leads to higher pressure in the top layer, thereby accelerating the downward motion of the PP1 fingers in the three frames of Fig. 21. Figure 22 shows the evolution of one such PP1 finger, which develops a blob at its tip, with a long neck, which tends to meander. Such drops at the tip of the fingers were already discovered in the 2D simulations by Tryggvason and Aref [17]. In this PP1-glycerin combination the interface

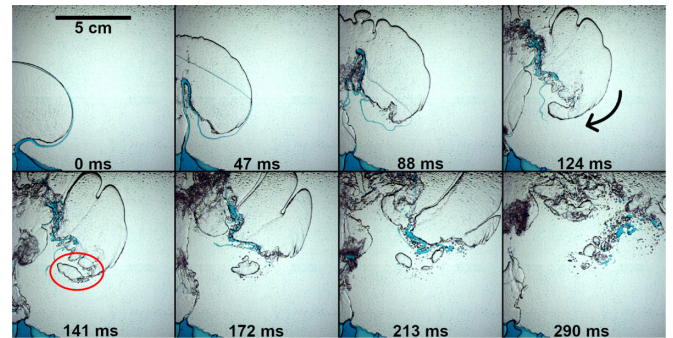


FIG. 23. The late stage of air-bubble breakup following its eruption through the pure glycerin layer, for $\Delta H_i = [0.25_a, 0.25_o, 0.25_g, 0.25_p]$. After the first eruption, sections from the bottom of the mushroom-shaped air finger will break into separated bubbles of different sizes, as highlighted with the ellipse in the fifth frame.

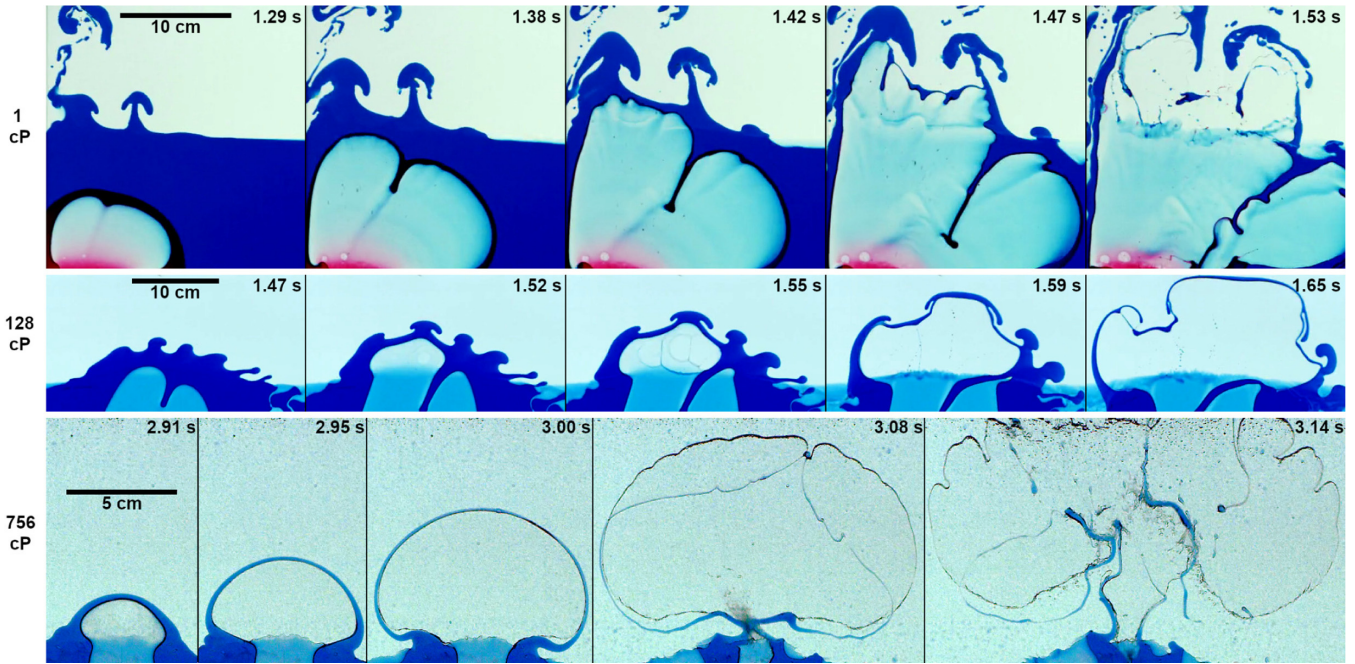


FIG. 24. The first air-finger eruptions through the blue glycerin-water layer for a range of greatly reduced viscosities, from those studied above in Figs. 4, 6, 10, etc. The viscosity values are listed on the left side. Note the film ruptures starting in the second panel of the middle row. All of the liquid layers have the same thickness of 25 %. For the water case $\mu_w = 1$ cP see Supplemental Video 6 [47], and for $\mu_g = 128$ cP see Supplemental Video 7 [47].

viscous Atwood number is $A \simeq 1$, i.e., one layer is much more viscous than the other. This is consistent with the trends in the finger shape as $A \rightarrow 1$ in their Figs. 3 and 4 [17].

The top of the expanding air-bubble becomes unstable to Rayleigh-Taylor instability, when the interface slows down. Undulations followed by fingers are visible from panel 8 in Fig. 12. The bottom section of the erupting mushroom shape also breaks up into many bubbles which enter the PP1 in the third row of this figure and close-up in Fig. 23.

For still lower viscosities μ_g the eruptions become more irregular with the blue ribbon above the bubble breaking up and the neck moving sideways in random fashion, as shown in Fig. 24. For the two lowest μ_g the upper interface has already developed mushroom-type instabilities, which are stretched by the erupting bubble. From our experiments the regular air eruptions persist for $\mu_g = 570$ cP, but are irregular below that.

D. Triple emulsions

The presence of four immiscible layers can lead to novel transient dynamics, with interactions where three or all four phases play a role. These we will describe only qualitatively, while a detailed characterization must await further study. We classify these as *channeling*, *cave filling*, and *patterning*.

1. Channeling

During the interchange of the air and PP1 layers, the air channels rapidly through the glycerin, via the erupting air fingers, studied above. Similarly, PP1 fingers descend, but often split into droplets, without forming a shortcut through the glycerin layer, thereby not being able to bypass the viscous stress of the surrounding liquid, which delays their motion.

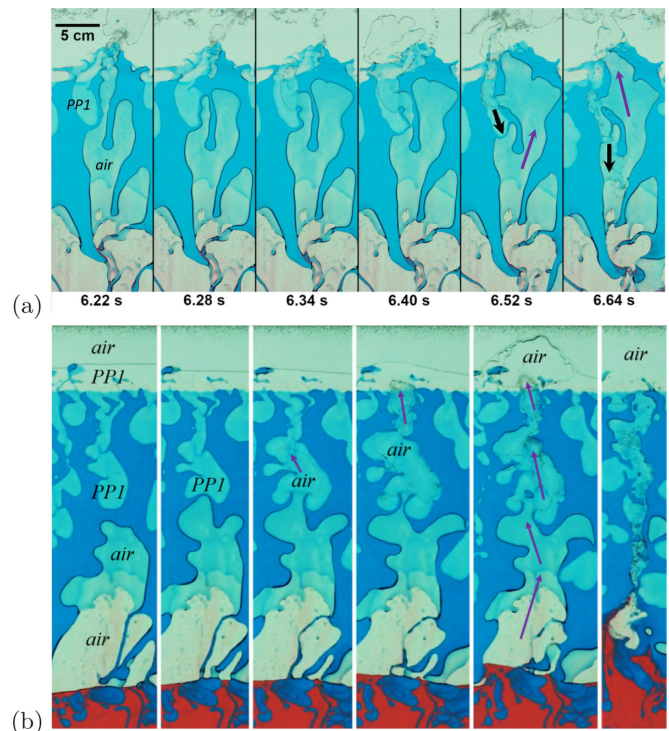


FIG. 25. (a) The channeling of a descending PP1 liquid blob into a rising continuous air finger, inside the blue glycerin layer, for $\Delta H_i = [0.25_a, 0.25_o, 0.25_g, 0.25_p]$. The black arrows show the descending PP1 and the purple arrows the rising air. See also Supplemental Video 8 [47]. (b) Channeling of air upward through a PP1 finger inside pure glycerin, for $\Delta H_i = [0.27_a, 0.25_o, 0.33_g, 0.15_p]$. See also Supplemental Video 9 [47].

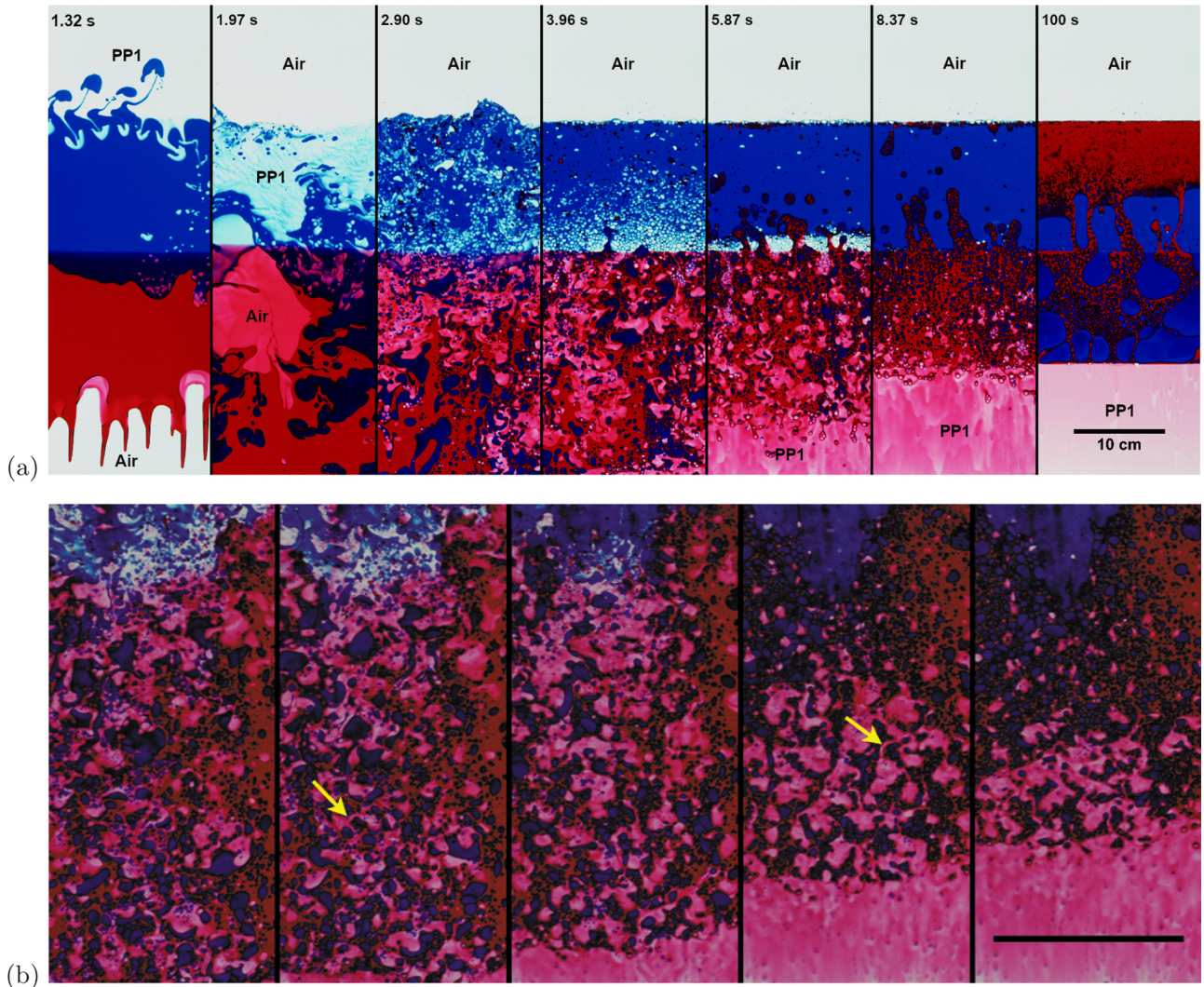


FIG. 26. (a) Overturning dynamics for the lowest-viscosity pure water in the blue layer. For equal layer depths $\Delta H_i = [0.25_a, 0.25_o, 0.25_w, 0.25_p]$. The vertical channels of red olive oil have numerous minute blue water droplets within. Keep in mind that the evolution is far from uniform along the width of the cell due to large overturning blobs of air and PP1. (b) Close-up of the filament formation (arrows) when the low-surface-tension PP1 is stretched around the blue water droplets inside the red olive oil continuous phase. Both scale bars are 10 cm. See also Supplemental Video 6 [47].

However, this can be bypassed if the PP1 liquid manages to enter the air-channel from the side. Figure 25(a) shows an example of this dynamic. Here a PP1 finger enters a continuous air-channel from the side and thereafter falls rapidly within it. Figure 25(b) shows a similar process, where a rising air finger meets a falling PP1 finger and quickly rises through it. This occurs much faster than the air finger rising through the viscous glycerin and the large air pocket escapes rapidly leaving behind a collapsed channel in the last panel. Dark patches of PP1 spray are visible in the last two panels.

During the later stage, when the two middle intermediate-density layers of oil and glycerin interchange, this occurs much more slowly on account of the larger viscosities and the smaller density difference. The oil is 146 times more viscous than the PP1 and the density difference between the olive oil and glycerin is only $\rho_g - \rho_o = 341 \text{ kg/m}^3$. This interchange can be quite irregular with countermoving blobs of opposite liquids, as shown in Fig. 6. However, for the lowest viscosity

pure water without glycerin, Fig. 26, we again see prominent channeling. However, in contrast to the earlier air-channels, where the air is of much lower viscosity than the surrounding water-glycerin, here the channel fluid is of higher viscosity than the surrounding one, i.e., channels of olive oil within the water in the last panel of Fig. 26(a). These channels appear to be stabilized by the internal emulsion droplets of water within the oil, which prevent pinch-off of the channels. These water droplets are pulled upward by the viscous stress against their downward buoyancy.

This interchange of the middle layers is compared in more detail in Fig. 27 for pure water in Fig. 27(a) and pure glycerin in Fig. 27(b). For the water case, the panels and associated Video 10 show the persistence of these narrow channels. The lower panels in Fig. 27 show the vertical profiles of horizontal averages of the area fractions versus time, which are a strongly nonmonotonic functions of the depth, as seen for example by the localized peak in the green curve in Fig. 27(a). This arises

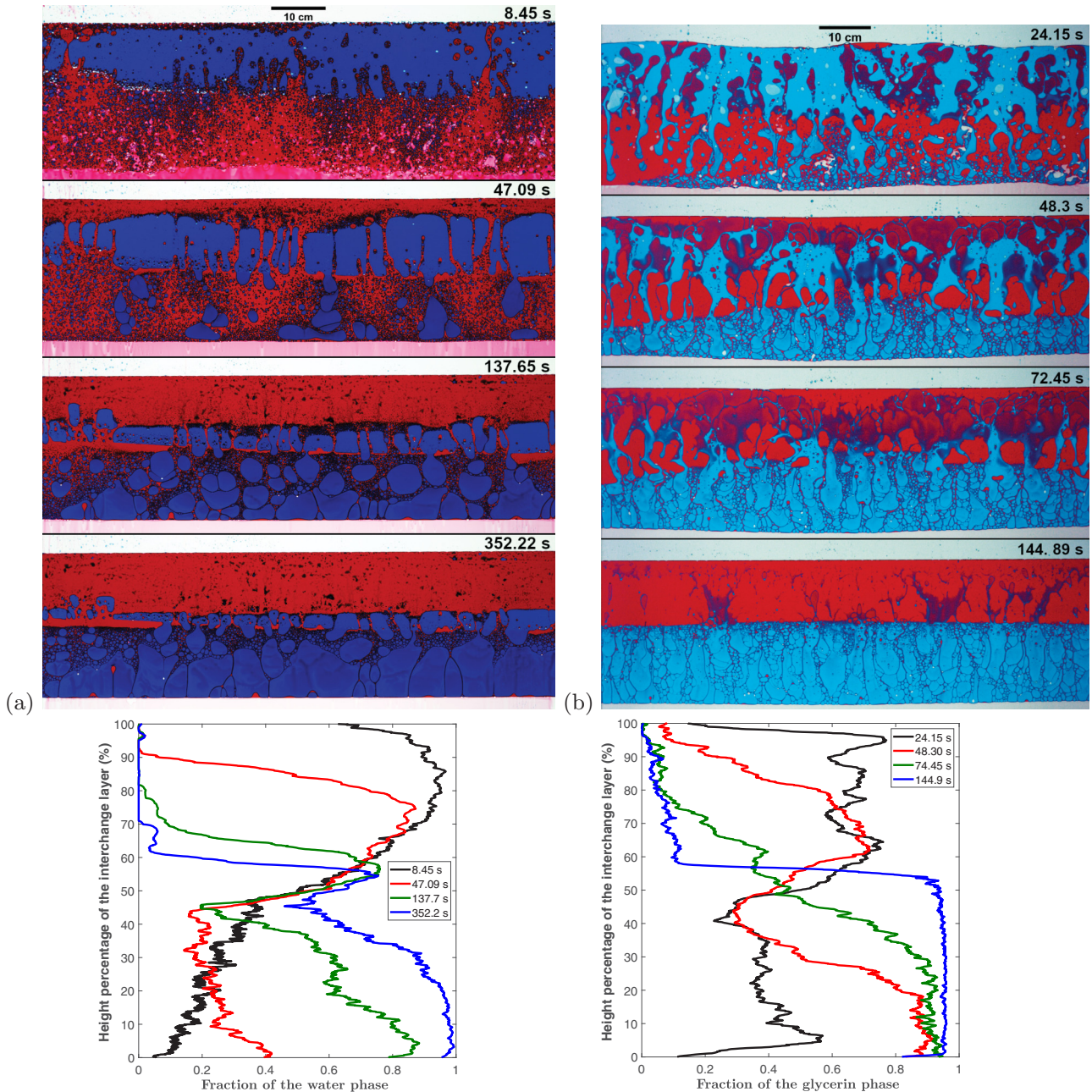


FIG. 27. The interchange of the two middle layers during the later stages after the overturn, for the two extremes in viscosity of the glycerin-water layer. (a) Blue layer is pure water with 1 cP viscosity, see also Supplemental Video 10 [47]. (b) Blue layer is pure glycerin with 1296 cP viscosity, see also Supplemental Video 11 [47]. The image strips show only the middle two layers. The bottom profiles show the horizontal average of the liquid fraction of the blue layers.

from the red oil flowing up along the channels, while the blue blobs of water slowly sink over the entire intermediate span. For the viscous glycerin in Fig. 27(b) the interchange is more even, but with downward motions in prominent but wider blue glycerin channels.

2. Cave filling

The phenomenon we refer to as “cave filling” is when the low-viscosity PP1 can enter the air pockets within the higher-viscosity glycerin. Figures 28(a) and 28(b) show examples of this. Figure 28(a) shows the interaction of a rising bubble

and a falling PP1 finger. The tip of the PP1 is pulled in by the induced flow of the bubble and enters its trailing edge filling its bottom section. The hydrostatic pressure inside a bubble is constant and as it rises it pulls the PP1 liquid up along the channel, as indicated by the arrows, with some PP1 liquid reaching up to the original PP1 layer. Keep in mind that the average density of air and PP1 is lower than that of the surrounding glycerin layer, i.e., $(\rho_a + \rho_p)/2 < \rho_g$, at $856 < 1260 \text{ kg/m}^3$.

Figure 28(b) shows a second case, where the PP1 liquid invades an air bubble from the bottom, rising and sloshing within it until it forms a flat surface.

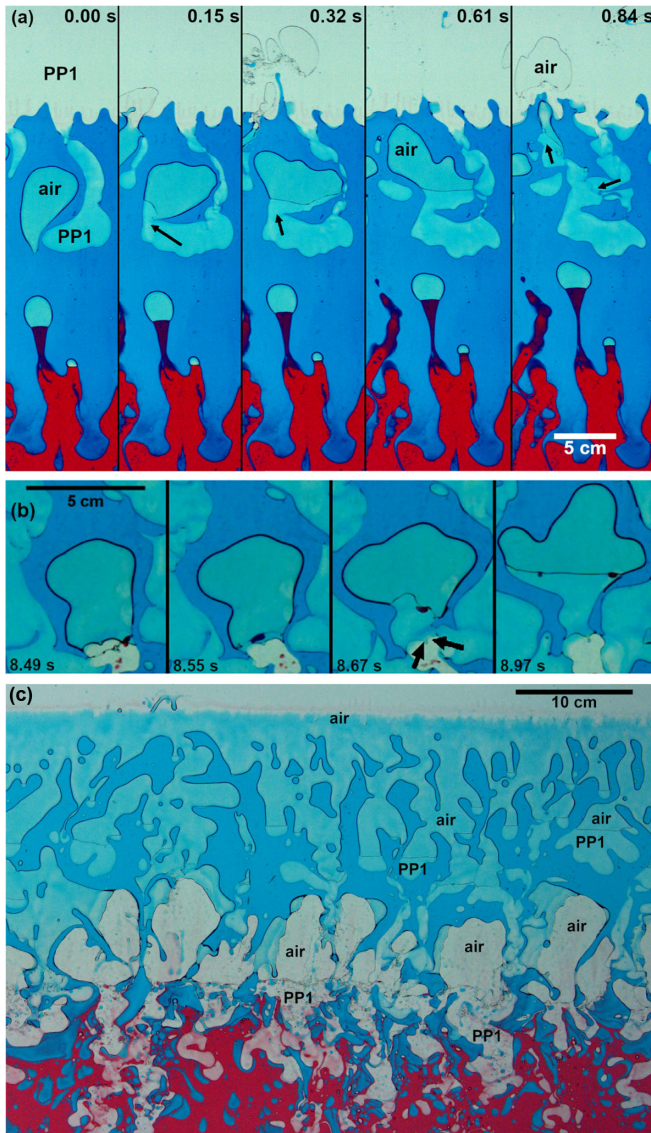


FIG. 28. [(a), (b)] Examples of *caving* for $\Delta H_i = [0.09_a, 0.25_o, 0.33_g, 0.33_p]$. The arrows point out the flow of PP1 liquid into the air pockets. See also Supplemental Video 12 [47]. (c) Channeling of the air into excavated channels in the glycerin. This occurs when the PP1 layer is narrower than the air layer $\Delta H_i = [0.35_a, 0.25_o, 0.25_g, 0.15_p]$. See also Supplemental Video 13 [47].

Figure 28(c) presents a different scenario appearing when there is a much deeper air layer than PP layer inside the cell. Here we see the air move downward into the channels in the glycerin left by the descending PP1. In other words the volume of air in the erupting air pockets overfills the head-space left by the original PP1 layer and follows it down the PP1 fingers before they can close up by hydrostatic pressure in the highly viscous glycerin. Flat air-PP1 interfaces are clearly visible inside many of the fingers.

3. Patterning of complex emulsion for lowest-viscosity water layer

Using low or zero concentration of glycerin in the glycerin-water layer we can reduce μ_g to that of water, or to match the viscosity of the olive oil layer. When the two middle layers are

of similar viscosity, which is still much higher than that of the top PP1 and bottom air layers, the rearrangement can occur by the interchange of PP1 and air, while the center of mass of the two middle layers have not moved much relative to each other. This certainly occurs in a very complex manner, without the well-defined air-finger eruptions. Figure 26(a) shows these dynamics for pure water in the blue layer. The second panel shows large blobs of both air and PP1 moving through the middle layers. The air moves most rapidly, reaching the top to form a gravitationally stable layer by the third frame. This is mostly due to its low density, but in part owing to the large surface tension between the air and liquids, which reduce the formation of small bubbles. These interactions leave a interacting emulsion of the three remaining liquids, with droplets of each one of them in the other, as shown in Figs. 26(b) and 27, making it somewhat ambiguous to determine which are the continuous or disperse phases.

Perhaps the most striking aspect of these motions is the patterning and tendrils formation when the PP1 drops descend inside the olive oil and stretch around the smaller water droplets. This is shown in Fig. 26(b), where arrows point out a couple of examples, see also Supplemental Video 6 [47].

E. Three layers

While our study has concentrated on four-layer configurations, keep in mind that bubble eruptions will also occur in a three-layer setup without the olive oil layer. We have verified this in a separate set of experiments. One of these realizations is shown in Fig. 29 and Supplemental Video 14 [47], where all three layers are of equal depths, of air, glycerin, and PP1.

The Rayleigh-Taylor instability develops much earlier on the bottom interface (glycerin over air), with the dominant air finger penetrating the entire glycerin layer before the top interface (PP1 over glycerin) forms any clear undulations. This is consistent with predictions of Eq. (9) as described at the start of Sec. V B. Furthermore, one notes that the contact line at the bottom of the main finger remains steady at the location of the original interface, during the rapid rise of the finger.

The eruption of the air finger in the fourth panel looks similar to those in the four-layer configurations, with a tendril of glycerin above it. The PP1 descends in a more chaotic manner breaking into numerous blobs in panels 6–8, which shifts some of the glycerin downward, after all the air has reached the top. Keep in mind that in this setup, the interchange of air and PP1 could occur without the glycerin displacing at all in the vertical direction.

VI. DISCUSSIONS AND CONCLUSIONS

Herein we have performed experiments of gravity-driven immiscible multilayer flow inside a Hele-Shaw cell. These experiments show examples of many multiphase phenomena well-studied in other configurations. The four-layer system investigated has also revealed unexpected dynamics. For example, we see the rapid interchanging of the top and bottom layers without the middle two layers overturning. This is clear from the overall images, but also by the trajectories of the center-of-mass of those two middle layers, as shown in Fig. 7(a). Our focus is on air-eruptions when buoyancy-driven fingers penetrate through a viscous

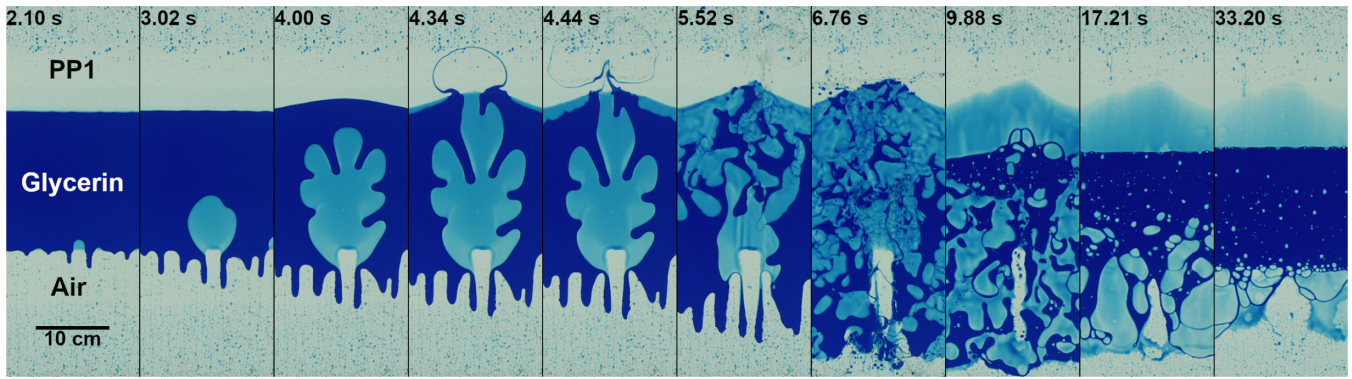


FIG. 29. Eruption and interchange dynamics for a three-layer system, with bottom air, top PP1 and pure glycerin in the middle blue layer. $\Delta H_i = [0.34_a, 0.33_g, 0.33_p]$. See also Supplemental Video 14 [47].

glycerin layer into the lower-viscosity PP1 layer. An emerging theme we observe is the importance of channeling during the rearrangement of the various immiscible fluid layers. Such channeling bypasses the imposed flow-restriction by larger-viscosity layers. This demonstrates clearly the limitations of applying one-dimensional modeling of the flow of emulsions in multilayer systems, which can appear in industry and geophysics.

While we have only studied a few of the myriad of possible multilayer configurations, we expect similar dynamics to emerge in many others. Just as a prominent viscous finger dominates a two-layer Hele-Shaw flow [2,18], we observe isolated eruptions control the interchange of layers which are separated by other more viscous layers.

We successfully model the eruption of the air finger, into the low-viscosity PP1 layer, as a 2D inertial process, assuming a constant driving pressure. The best fit pressures show consistent trends with the overpressure, of the bottom air source, from the overlying PP1 and glycerin layers [Fig. 15(c)]. The over-pressure is moderated by the fully enclosed cell, as discussed in Sec. VC 1. The high-speed airflow in the narrow channel moves at ~ 1 m/s, derived from the volume change of the erupting bubble, but speeds up during the neck pinch off, when the neck area reduces greatly. This dislodges fine spray from the wetting films on the walls, when the air velocity in the neck reaches ~ 20 m/s. The high-speed video tracks the fastest microdroplets at up to 4 m/s, ejected upward through the growing bubble.

The rapid airflow leads to periodic pinch-offs near the top of the channel, where it is usually narrowest. This is primarily driven by hydrostatic pressure but accelerated by the suction Bernoulli pressure near the final pinch-off. The frequency of these repeated pinch-offs is determined by local dynamics and appear insensitive to the layer depths of the PP1 or glycerin-water layers. The larger viscosity shows slightly more frequent pinch-offs, suggesting that viscous stress does not play a controlling role in this process. This phenomenon is reminiscent of the intermittent pinch-off of air which occurs during the pouring of liquid out of a bottle, which produces the familiar *glug-glug* sound. In that case the liquid impacts on the glass wall. Clanet and Searby [45] studied these dynamics in an idealized bottle, in the form of a circular cylinder with a hole in a thin horizontal partition, where bubbles are released during the draining. Direct comparison with this seminal

study is difficult as the size of the neck of our air finger is not fixed, as their hole diameter.

The relatively large spacing of the glass plates, along with different wetting properties of the various liquids, means that there will be liquid films along the walls, underneath the droplets or blobs of other liquids rising or falling vertically. This makes the fine-scale flow more three-dimensional and not the typical 2D Hele-Shaw flow. The most significant effects of this is the change in boundary conditions, where the no-slip in the viscous layers can be relaxed. Possible contact lines also add local forces affecting the motions. The viscous ribbon stretched out over the erupting air bubble, is another characteristic feature which reveals the three-dimensionality when the air finger bypasses it when it becomes too thin, as is shown in Figs. 12 and 14(b). Finally, the observed spray formation from the high-speed airflow along the PP1 films has droplet diameters orders of magnitude smaller than the gap size. While this complicates the description of the flow, in real flows such films are often present and should not be ignored in the modeling.

Herein we have selected to study four immiscible layers, but bubble eruption also occurs for only three layers, as was shown in Fig. 29. The four-layer configuration gives rise to three- and four-phase interactions shown in Sec. VD. One additional benefit of the four layer setup is reducing the initial disturbance of the bottom of the glycerin layer, caused from the rotation of the Hele-Shaw cell. Gertsenshtein *et al.* [46] have established that initial disturbance will impact both the amplitude as well as the growth rate of the fingers.

In contrast to the smooth branching of the rising air fingers, the falling PP1 streams are susceptible to a meandering instability, as shown in Fig. 22.

In conclusion, our results highlight the importance of channeling in multilayer flow in a Hele-Shaw device. This system can serve as a testbed for multiphase flow relevant to industry and geophysics.

ACKNOWLEDGMENT

This work was funded by King Abdullah University of Science and Technology (KAUST) under baseline support No. BAS/1/1352-01-01.

- [1] H. M. Gonnermann and M. Manga, The fluid mechanics inside a volcano, *Annu. Rev. Fluid Mech.* **39**, 321 (2007).
- [2] P. G. Saffman and G. I. Taylor, The penetration of a fluid into a porous medium or Hele-Shaw cell containing a more viscous liquid, *Proc. R. Soc. London A* **245**, 312 (1958).
- [3] R. A. Wooding, Growth of fingers at an unstable diffusing interface in a porous medium or Hele-Shaw cell, *J. Fluid Mech.* **39**, 477 (1969).
- [4] C.-W. Park, S. Gorell, and G. Homsy, Two-phase displacement in Hele-Shaw cells: Experiments on viscously driven instabilities, *J. Fluid Mech.* **141**, 275 (1984).
- [5] C. Park and G. Homsy, The instability of long fingers in Hele-Shaw flows, *Phys. Fluids* **28**, 1583 (1985).
- [6] P. Saffman, Viscous fingering in Hele-Shaw cells, *J. Fluid Mech.* **173**, 73 (1986).
- [7] K. V. McCloud and J. V. Maher, Experimental perturbations to Saffman-Taylor flow, *Phys. Rep.* **260**, 139 (1995).
- [8] E. Pauné, M. Siegel, and J. Casademunt, Effects of small surface tension in Hele-Shaw multifinger dynamics: An analytical and numerical study, *Phys. Rev. E* **66**, 046205 (2002).
- [9] H. S. Hele-Shaw, The flow of water, *Nature* **58**, 34 (1898).
- [10] A. Huerre, O. Theodoly, A. M. Leshansky, M.-P. Valignat, I. Cantat, and M.-C. Jullien, Droplets in Microchannels: Dynamical Properties of the Lubrication Film, *Phys. Rev. Lett.* **115**, 064501 (2015).
- [11] P. Aussillous and D. Quéré, Quick deposition of a fluid on the wall of a tube, *Phys. Fluids* **12**, 2367 (2000).
- [12] I. Shukla, N. Kofman, G. Balestra, L. Zhu, and F. Gallaire, Film thickness distribution in gravity-driven pancake-shaped droplets rising in a Hele-Shaw cell, *J. Fluid Mech.* **874**, 1021 (2019).
- [13] B. Peck and L. Sigurdson, On the kinetics at a free surface, *IMA J. Appl. Math.* **61**, 1 (1998).
- [14] M.-J. Thoraval, Y. Li, and S. T. Thoroddsen, Vortex-ring-induced large bubble entrainment during drop impact, *Phys. Rev. E* **93**, 033128 (2016).
- [15] G. M. Homsy, Viscous fingering in porous media, *Annu. Rev. Fluid Mech.* **19**, 271 (1987).
- [16] R. B. Needham, P. H. Doe *et al.*, Polymer flooding review, *J. Petrol. Technol.* **39**, 1503 (1987).
- [17] G. Tryggvason and H. Aref, Numerical experiments on Hele-Shaw flow with a sharp interface, *J. Fluid Mech.* **136**, 1 (1983).
- [18] T. Maxworthy, The nonlinear growth of a gravitationally unstable interface in a Hele-Shaw cell, *J. Fluid Mech.* **177**, 207 (1987).
- [19] J. V. Maher, Development of Viscous Fingering Patterns, *Phys. Rev. Lett.* **54**, 1498 (1985).
- [20] D. Halpern and D. Gaver III, Boundary element analysis of the time-dependent motion of a semi-infinite bubble in a channel, *J. Comput. Phys.* **115**, 366 (1994).
- [21] R. Ledesma-Aguilar, I. Pagonabarraga, and A. Hernández-Machado, Three-dimensional aspects of fluid flows in channels. II. Effects of meniscus and thin film regimes on viscous fingers, *Phys. Fluids* **19**, 102113 (2007).
- [22] P. Daripa and G. Paşa, On the growth rate for three-layer Hele-Shaw flows: Variable and constant viscosity cases, *Int. J. Eng. Sci.* **43**, 877 (2005).
- [23] P. Daripa, Studies on stability in three-layer Hele-Shaw flows, *Phys. Fluids* **20**, 112101 (2008).
- [24] P. Daripa, Hydrodynamic stability of multilayer Hele-Shaw flows, *J. Stat. Mech.: Theory Exp.* (2008) P12005.
- [25] P. Daripa, On estimates for short wave stability and long wave instability in three-layer Hele-Shaw flows, *Physica A* **390**, 3069 (2011).
- [26] P. Daripa, On stabilization of multilayer Hele-Shaw and porous media flows in the presence of gravity, *Transp. Porous Media* **95**, 349 (2012).
- [27] P. Daripa and X. Ding, Selection principle of optimal profiles for immiscible multifluid Hele-Shaw flows and stabilization, *Transp. Porous Media* **96**, 353 (2013).
- [28] C. Gin and P. Daripa, A study of a nonstandard eigenvalue problem and its application to three-layer immiscible porous media and Hele-Shaw flows with exponential viscous profile, *J. Math. Fluid Mech.* **17**, 155 (2015).
- [29] C. Gin and P. Daripa, Stability results on radial porous media and Hele-Shaw flows with variable viscosity between two moving interfaces, *IMA J. Appl. Math.* **86**, 294 (2021).
- [30] C. Imrak and I. Gerdemeli, An exact solution for the deflection of a clamped rectangular plate under uniform load, *Appl. Math. Sci.* **1**, 2129 (2007).
- [31] A. B. Aljedaani, C. Wang, A. Jetly, and S. T. Thoroddsen, Experiments on the breakup of drop-impact crowns by marangoni holes, *J. Fluid Mech.* **844**, 162 (2018).
- [32] G. I. Taylor, The instability of liquid surfaces when accelerated in a direction perpendicular to their planes, *Proc. R. Soc. London, A* **201**, 192 (1950).
- [33] S. Chandrasekhar, *Hydrodynamic and Hydromagnetic Stability* (Dover, Mineola, NY, 1961).
- [34] S. Hill, Channelling in packed columns, *Chem. Eng. Sci.* **1**, 247 (1952).
- [35] R. Chouke, P. van Meurs, and C. van der Poel, The instability of slow, immiscible, viscous liquid-liquid displacements in permeable media, *Petroleum Transactions AIME* **216**, 188 (1959).
- [36] V. Duclaux, F. Caille, C. Duez, C. Ybert, L. Bocquet, and C. Clanet, Dynamics of transient cavities, *J. Fluid Mech.* **591**, 1 (2007).
- [37] A. R. Kopf-Sill and G. Homsy, Bubble motion in a Hele-Shaw cell, *Phys. Fluids* **31**, 18 (1988).
- [38] C.-W. Park, S. Maruvada, and D.-Y. Yoon, The influence of surfactant on the bubble motion in Hele-Shaw cells, *Phys. Fluids* **6**, 3267 (1994).
- [39] S. Maruvada and C.-W. Park, Retarded motion of bubbles in Hele-Shaw cells, *Phys. Fluids* **8**, 3229 (1996).
- [40] Y. Ling, J.-M. Fullana, S. Popinet, and C. Josserand, Droplet migration in a Hele-Shaw cell: Effect of the lubrication film on the droplet dynamics, *Phys. Fluids* **28**, 062001 (2016).
- [41] P.-G. De Gennes, F. Brochard-Wyart, and D. Quéré, *Capillarity and Wetting Phenomena: Drops, Bubbles, Pearls, Waves* (Springer Science & Business Media, Berlin, 2013).
- [42] E. Q. Li, S. Al-Otaibi, I. U. Vakarelski, and S. T. Thoroddsen, Satellite formation during bubble transition through an interface between immiscible liquids, *J. Fluid Mech.* **744**, R1 (2014).

- [43] E. Reyssat and D. Quéré, Bursting of a fluid film in a viscous environment, *Europhys. Lett.* **76**, 236 (2006).
- [44] Z. Jian, P. Deng, and M.-J. Thoraval, Air sheet contraction, *J. Fluid Mech.* **899**, A7 (2020).
- [45] C. Clanet and G. Searby, On the glug-glug of ideal bottles, *J. Fluid Mech.* **510**, 145 (2004).
- [46] S. Y. Gertsenshtein, I. Kozlov, V. Prokof'ev, N. Reznichenko, G. Chernyi, and V. Chernyavskii, Effect of initial disturbances on the Rayleigh-Taylor instability in a Hele-Shaw cell, *Fluid Dyn.* **43**, 341 (2008).
- [47] See Supplemental Material at <http://link.aps.org/supplemental/10.1103/PhysRevE.105.045101> for video clips.